University of Bergen
Department of Physics and Technology

Charged Jet Spectra in proton-proton collisions at $\sqrt{s} = 13$ TeV with ALICE

Author: Sivert Olsen Løvaas
Supervisor: Dieter Rudolf Christian Röhrich
Co-supervisor: Ingrid McKibben Lofnes

UNIVERSITETET I BERGEN
Det matematisk-naturvitenskapelige fakultet

Master in Experimental Particle and Nuclear Physics
October, 2022

Abstract

The ALICE experiment was designed mainly to study the formation of the exotic, very hot and very dense state of matter known as the Quark Gluon Plasma (QGP), which occurs in Pb-Pb collisions. An important probe to form a basic understanding of the strong interactions in the QGP is the study of proton-proton collisions.
In this thesis, the charged jet cross section at mid-rapidity produced in proton-proton collisions at center-of-mass energy $\sqrt{s} = 13$ TeV will be studied. The analyzed data sample includes a total of 12 million minimum bias triggered events from LHC run 2, collected in ALICE during the period from 2017 to 2018. A further subsample of 1,7 million Transition Radiation Detector triggered events has also been analyzed. Jets are reconstructed using the anti-kt algorithm, and the raw spectra is unfolded using the Bayesian method.

Acknowledgements

I would like to thank my main supervisor Professor Dieter Röhrich for the opportunity to work in this interesting field of physics and for your advisement along the way.
To Ingrid Lofnes, I would very much like to thank you for your patience with me, all my repeated questions, and generally unorganized work structure. I have really appreciated your continuous encouragement and praising of even the smallest achievements. And thanks to both Ingrid, Amalie Hovland and Andreas Handeland for proofreading my thesis, providing both important formal corrections and several good suggestions. I would like to thank Constantin Loizides as well, for revitalizing my interest and understanding of detector physics in the Experimental Methods in Nuclear and Particle Physics course. I really don't think I would have been able to complete that course without his engaging style of online lecturing during that dreaded Covid-19 lockdown period. Lastly, I would like to thank my whole family, and my parents especially, for the unceasing support and encouragement throughout all of my university studies. And even to Luci, my little demon kitty, thanks for reminding me to have fun sometimes, even when the going gets tough, and also for waking me up extra early in the morning.

Sivert Olsen Løvaas
Friday 7$^{\text{th}}$ October, 2022

Contents

List of Figures

List of Tables

Chapter 1

Introduction

In humanity's quest to understand the universe, what it is made of and how it functions, we have come a long way from where the philosophy of the atomos started some 2400$\sim$ years ago. The last hundred years have seen an explosion from the very basic understanding of the structure of the atom, to what we today call the Standard Model of particle physics. Many of the important discoveries made in this field of science is due to experiments done at the European Organization for Nuclear Research, best known as CERN[1], using the Large Hadron Collider (LHC). Physicist have concluded that during the very earliest moments of the Big Bang, the universe was in a state known as a quark-gluon plasma. In heavy ion collisions at the LHC, this state of matter is recreated, and its byproducts are recorded in massive detector structures, one of which is known as A Large Ion Collider Experiment, or more commonly referred to as ALICE. This incredibly hot and dense state of matter, at some 5.5 trillion degrees, is the hottest thing ever created on earth. It is even 100'000 times hotter than the center of the sun.

From its early days, ALICE have been through many upgrades, and are now colliding (among other particles) protons at a center-of-mass energy up to $\sqrt{s} = 13$ TeV. These proton-proton collisions serve as an important probe in the study of other collision types, as the proton-lead or lead-lead collisions, from which we create the deconfined state of matter called the quark-gluon plasma. From the initial hard collisions, a phenomenon known as *jets* occurs. Jets, briefly stated, are highly energetic showers of collimated particles originating from the same source. In cases where the jet event occurs near the edge of the deconfined medium, jets effectively serve as partonic probes of the quark-gluon

[1]The name CERN is derived from the acronym for the French "Conseil Européen pour la Recherche Nucléaire".

plasma, since they are energetic gluons and quarks traversing a colored medium. Thus, the properties of the quark-gluon plasma can be studied by comparing the jet readout from collisions with and without the deconfined medium occurring. Jet events in vacuum, i.e., without the quark-gluon plasma forming, is found through pp collisions. To do this, jets need to be experimentally defined, detected and analyzed.

In this thesis, we will study charged jets at mid-rapidity in data recorded by ALICE at the LHC. Data from data taking run 2 is used, recorded during 2017 (LHC17) and 2018 (LHC18). The measured, raw jet p_{T} spectra is extracted. The measured spectra are then unfolded to take into account the error from recording limitations, such as diffusion and detector acceptance. The jet p_{T} spectra are extracted using an analysis framework developed for the analysis of J/ψ mesons decaying into leptons, as a case study for the future analysis of J/ψ tagged jets. The analysis presented in this thesis provides the groundwork for further studies of heavy flavor tagged jets, especially configured for the search for J/ψ candidates in jets.

Chapter 2

Theory

2.1 Quantum ChromoDynamics

The theory describing the strong interaction is known as Quantum ChromoDynamics (QCD). Chromo, meaning color, refers to the so called 'color charge' of the strongly interacting constituents of particles, namely quarks and gluons. Quarks are the fundamental constituents of hadrons, with the most known examples being protons (uud) and neutrons (udd), and gluons are the fundamental force carrier of the strong force. Both the quarks and the gluons carry color charge, which is not to be confused with the electric charge of Quantum ElectroDynamics (QED). There are, however, several similarities in the underlying theory. The fundamental difference lies in the non-binarity of the color charge. Instead of only positive and negative, in a sense one direction and its counterpart, the color charge instead has three 'directions', known as red, green or blue. These directions describe the orthogonal states in the SU(3) color space, which is the gauge field used to describe QCD in terms of field theory [1]. A parton, that is a gluon or quark, may instead also carry the color anticharge, that is anti-red, anti-green or anti-blue. Quarks combine in either pairs (mesons) or in triplets (baryons). A condition for the combination of quarks into hadrons is the color neutrality of the combination, a so-called 'color singlet'. This is done either from all the colors red, green and blue, being combined, or from any one color and its color anticharge.

There are two main distinguishing features of the QCD theory, namely *confinement* and *asymptotic freedom*. In the following three subchapters, we will take a look at the lagrangian of the QCD theory, as well as the two aforementioned features.

2.1.1 The Lagrangian of QCD

The gauge invariant Lagrangian for QCD can be written as follows:

$$\mathcal{L} = \bar{\psi}[i(\gamma^\mu D_\mu) - m]\psi - \frac{1}{4}G_{\mu\nu}G^{\mu\nu}\,. \tag{2.1}$$

Here, the ψ is the Dirac spinor for the quark field, D_μ is the covariant derivative ensuring gauge invariance in SU(3) transformations, with m being mass and $G_{\mu\nu}$ representing the gluon field strength tensor, containing the gluon self-interaction. SU(3) can be thought of as the directions of the color charge space, or 'flavor space', as mentioned in section 2.1. The gluon self-interaction is described in theory by the non-commuting relation of the SU(3) generators, i.e., QCD is a non-Abelian gauge theory [1].

2.1.2 Confinement and The Hadronisation process

One of the most important distinguishing features of QCD, making it distinctly different from QED, is the reason for and consequences of *confinement*. While the electrons of QED are free to move around (given enough energy) and can break free from any bond, releasing them as electrical current or beta radiation, an equivalent is not found for the quarks of the QCD theory. The quarks are, with some very outlying exceptions, confined to hadrons of two or three quarks [15].
Three quark confinement, i.e., in a baryon, must be treated as a relativistic three-body problem [16], and is beyond the scope of this thesis, and also less relevant. In mesons, a simpler two-body problem, confinement comes from the potential between a heavy quark and an anti-quark. This potential can be described in the form of the Cornell potential, given here in Equation (2.2) [17].

$$V_{q\bar{q}} = -\frac{4}{3}\cdot\frac{\alpha_s}{r} + k\cdot r\,, \tag{2.2}$$

where $k \approx 1$ GeV/fm is the linear string strength [18, 19].

The first term in Equation (2.2) is known as the Colombic term, with distance r and the value for the gauge coupling factor α_s. This α_s factor, ironically often referred to as

the α_s constant, although it is in fact not constant but instead dependent on the radius of the studied hadron. Its value typically ranges from 0.19 to 0.4 [20].

The second term, containing the linear string strength k, is the linear confinement term. As distance increases, this term dominates, and the potential energy increases linearly with distance. Specifically, if distance is to be increased to infinity, the required energy to do so would also have to be infinite. At a given distance, the energy becomes so large that it is energetically favorable to create a new quark anti-quark ($q\bar{q}$) pair, which has to be color neutral. One way of thinking of this strong-force interaction is by imagining a rubber band. The ends of this rubber band are the quark and the anti-quark, while the force transversing the band are virtual gluons. As the band is stretched further apart, the energy increases until it suddenly snaps. Unlike a real rubber band, however, this QCD band repairs the ends of the now two rubber bands by creating a new quark anti-quark pair. This new pair combines with the distanced pair, and creates a new hadron. This hadronisation process is known as *confinement* and is visualized in Figure 2.1 [1]. Due to this process, single quarks are generally not freely moving around, and the quarks are never directly observed as free unbound particles. As further discussed in Section 2.2, the quark become quasi-free in the Quark-Gluon Plasma (QGP). One other interesting result of the dynamics of such hardronisation, is the production of so-called dijet. In the rest frame of the original meson, the first two rehadronised particles will travel in diametrically opposite directions. If the quark pair has enough energy to continue the splitting and rehadronisation process, two jets, i.e., a dijet, will ensue. Thus, dijets are always produced back-to-back, and the readout will be seen with a high degree of geometric symmetry in the azimuthal angle.

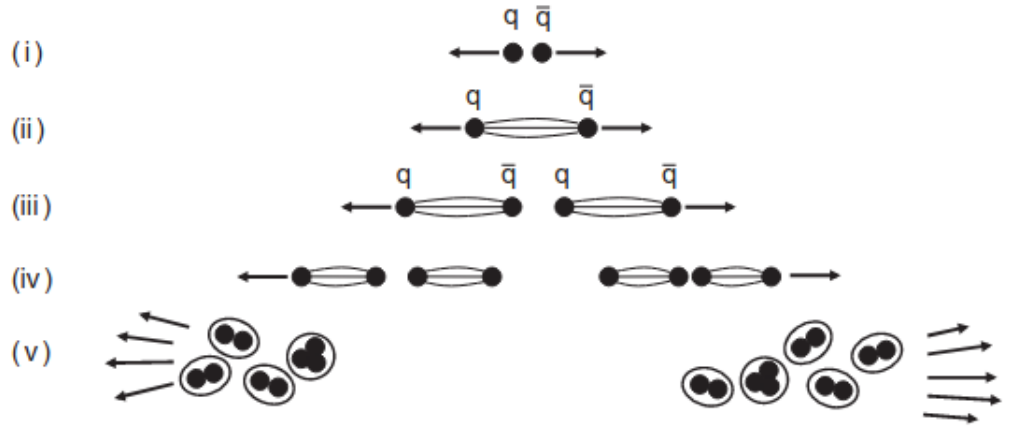

Figure 2.1: A qualitative picture of the fragmentation and rehadronisation process of two quarks being pulled apart. In the initial state (i), the quarks are still part of a meson. As energy is added to the system, and the quarks are pulled apart (ii), a column of gluons is created. At some point (iii) it is energetically favorable to create two new quarks. If energy is high enough (iv), the splitting continues, and a dijet ensues (v) [1].

2.1.3 Asymptotic freedom and the running coupling factor

The second distinguishing feature of the QCD theory is asymptotic freedom, proposed by David Gross and Frank Wilczek [21], as well as separately by David Politzer, both in 1973 [22]. They were all awarded the Nobel Prize in Physics in 2004 for this prediction. The question posed is what happens when you go the other way, i.e., when distance r decreases and goes towards zero. The answer turned out to be that the charges enter each others charge cloud, and counteract the anti-screening effect and weaken the potential. The quarks then become quasi-free particles, unlike in their confined form. Experimental results indicate that with distances smaller than then the size of a hadron, the quarks move freely. The momentum transferred between quarks become very large with small distances because of the uncertainty relation $\Delta r \Delta p \geq 2\hbar$. One may then apply perturbative QCD (pQCD) to the QCD Lagrangian, Equation (2.1), to get what is known as the running coupling factor. With large momentum transfer at small distances, the running coupling factor becomes possible to estimate in terms of momentum transfer Q [22, 19]:

$$\alpha_s(Q^2) = \frac{\alpha_s(\mu^2)}{1 + \beta_0 \alpha_s(\mu^2) \ln(Q^2/\mu^2)}\,, \tag{2.3}$$

where β_0 is the first order perturbative coefficient for the given QCD configuration of quark flavors and colors, and is known as the 1-loop beta-function coefficient, and where $\alpha_s(\mu^2)$ is the coupling factor at a given transfer μ^2. With N_c being number of colors, and n_f the number of flavors, we have:

$$\beta_0 = \frac{11N_c - 2n_f}{12\pi}\,. \tag{2.4}$$

Experimentally, the coupling factor is commonly determined as $\alpha_s(M_z) = 0.1185 \pm 0.0006$ [23][1]. In particular, in the region around $|Q| \approx 1\,\text{GeV}$, α_s is of the order of one, and perturbation theory is not valid. Above 100 GeV, the typical scale for high-energy collision experiments, α_s is of the order of 0.1, and pQCD can be used. In contrast with pQED, the contributions from higher than first order corrections can not be neglected. Thus, we almost always see calculations beyond first order [1]. This is exemplified in the calculations used for all of the data points of Figure 2.2. This running coupling factor formula is in good agreement with the measurement of several different experiments. The relevant results can be seen in Figure 2.2 [1].

[1]referred to in [23] (pp. 122-134) as the "world average". Several calculations and experimental results have been used to come to this number. The other results than that of the lattice calculation has higher uncertainties, however, average at a within 0.2 standard deviations with the lattice result. Lattice calculations have thus played the role in "world average" of halving the uncertainty.

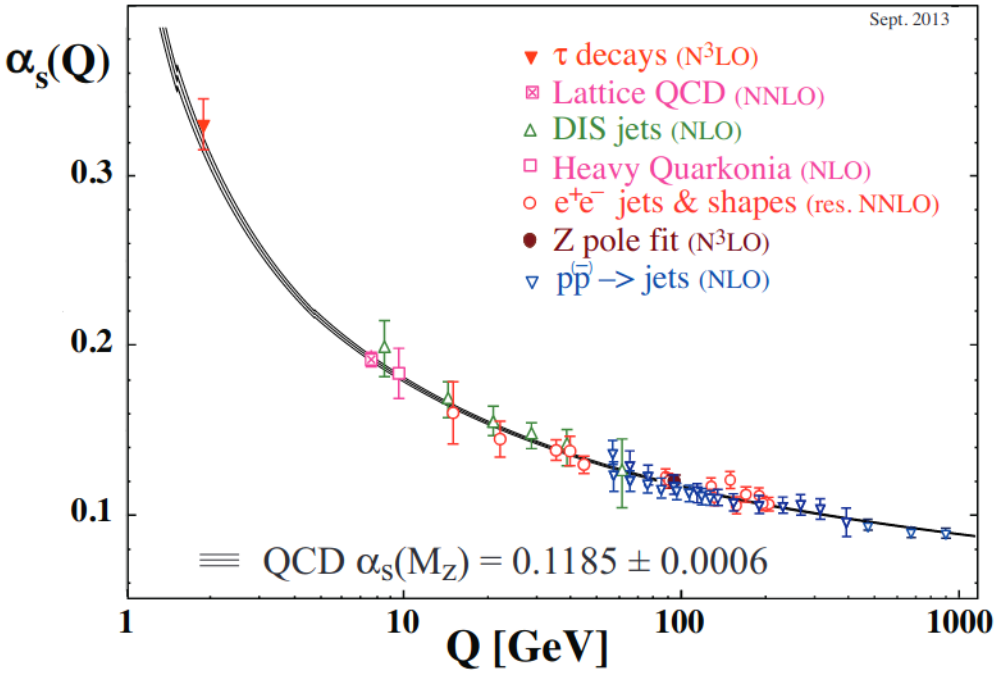

Figure 2.2: Several results of measurements of the running coupling factor in QCD, as a function of energy scale Q. The respective degree of QCDp used in the extraction of α_s is indicated in brackets(NLO: Next-to-Leading Order; NNLO: Next-to-Next-to-Leading Order; res. NNLO: NNLO matched with resummed next-to-leading logs; N^{3}LO: Next-to-NNLO) [1].

The n_f in formula (2.4) depends on the number of active flavors at the energy scale, i.e., flavors with mass $m_q < Q$ [22][19].

The methods developed for pQED can only be applied while the coupling factor is sufficiently less than unity. At high energies, this holds true, and perturbative calculations are used. At small energies, where α_s is increasing, it is possible to use lattice QCD (LQCD) calculations to calculate QCD properties [24].

2.1.4 Phase diagram of QCD

A thermodynamic treatment of QCD calculations indicate possible phase transitions for quarks approaching sufficiently high temperatures, or sufficiently high densities. In these conditions, the hadrons deconfine and the collection of particles enter into a state known as the Quark Gluon Plasma.

The strongly interacting particles are expected to exist in different states, depending on temperature T and baryochemical potential μ. The definition of μ is the energy

E needed to increase the total number of baryons and anti-baryons, such as protons and anti-protons, by one unit. This potential increases as density increases, i.e., as the average distance between the baryons decrease. As the QGP is still a topic of interest and investigation, the specific scales of the appropriate phase diagram is not yet know. For the time being, a schematic phase diagram has been proposed, as seen in Figure 2.3. The exact transitions for low temperature and increasing μ is not yet known, although a region of color superconducting matter is hypothesized. The critical energy density for the phase transition is $0.7 \pm 0.2\,\mathrm{GeV/fm^3}$ [25]. This critical energy density is about five times that of nuclear matter. For high temperatures and vanishing baryochemical potential, a crossover-region is expected. There are no first principles exact calculation, nor clear experimental results, for the values and behavior in the crossover region. Through LQCD, a region of about 150-170 MeV is expected for low μ. For reference, a temperature of 100 MeV is somewhat more than 1 trillion Kelvin, at $1.16 \cdot 1012\,K$ [25]. As seen in the Figure 2.3, ALICE energies result in exploration of a $T - \mu$ region above the crossover region.

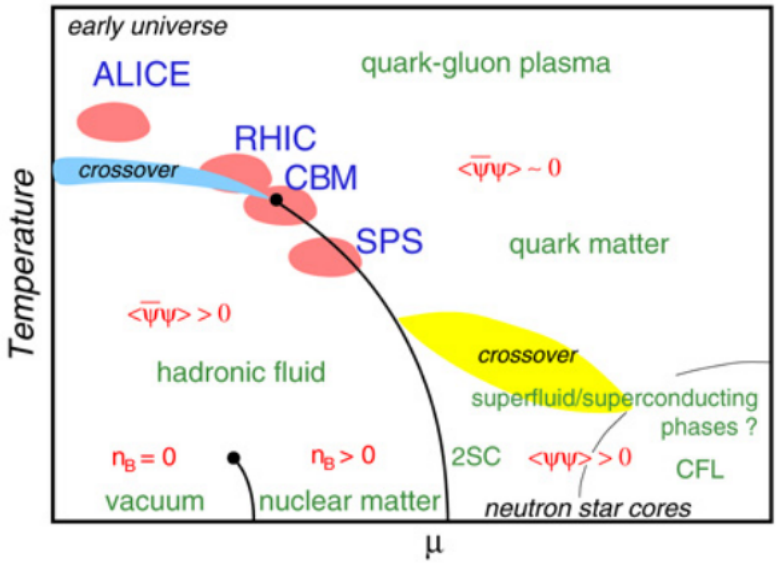

Figure 2.3: Phase diagram of nuclear matter. The axis are temperature versus baryochemical potential. Sufficient increase in either temperature or potential will lead to the formation of Quark Gluon Plasma. Normal, everyday conditions are vanishing in both regards [2].

2.2 The Quark Gluon Plasma

At extremely high temperatures, the formation of matter known as Quark Gluon Plasma (QGP) has been proposed. The properties of this very hot and very dense state of matter

is still a topic of great interest and investigation in modern particle physics. This can be seen in the upper right part of the phase diagram of figure 2.3.

The first signs of the QGP was found by the Super Proton Synchrotron (SPS) in the 1990s [26]. Later, the Relativistic Heavy Ion Collider (RHIC) was developed to study heavy ion collisions – and was at the time of construction (y2000) the highest energy collider of that type, surpassed only by the LHC in 2010 [27]. The QGP was observed by experiments at both RHIC and LHC, and the first findings of LHC are consistent with the findings of both RHIC and SPS. One surprising discovery made with RHIC is that the QGP acts as a perfectly frictionless liquid, as opposed to the expected behavior of a gaseous substance. The initially expected gaseous behavior was based on the assumption that any matter with pressures at large fractions of the Stephan-Boltzmann limit would act like a gas. The QGP was only expected to be weakly interacting, but given the magnitude of elliptic flow and the centrality dependence of particle production at high transverse momentum, it was concluded that the QGP had to involve other types of interactions as well [26].

As mentioned earlier, the first signs of the QGP was discovered by experiments at the SPS, and then later again at RHIC. The very first presentation of these results was at the turn of the millennium[2], early in the year 2000, where SPS at CERN presented the results of Pb-Pb-collisions of center-of-mass (CoM) about 17,2 GeV per nucleon pair [28, 24]. At the same time, the RHIC was developing dedicated experiments for examining the QGP, accelerating gold-nucleons to the point of reaching collision CoM at $\sqrt{s_{NN}} = 200$ GeV, servicing four experiments called BRAHMS, PHENIX, PHOBOS and STAR [25]. In 2010, LHC entered the contest, colliding lead nuclei at up to 2,76 TeV, subsequently upgrading acceleration to reach collisions of up to 5,02 TeV in 2015. In addition, LHC has a high energy proton-proton program, which serves as an important baseline for QGP studies.

2.2.1 Formation of QGP

High-energy accelerators are built to accelerate nucleon-beams to relativistic velocities, focusing opposing beams at the collision point where the QGP is expected to form. Due to relativistic velocities, the nuclei become Lorenz-contracted, approaching each other as more or less flat discs. As they collide, an important factor for the resulting "fireball", is

[2]arguably, just before the turn of the millennium: https://www.scientificamerican.com/article/when-is-the-beginning-of/

the centrality of the collision. The relevant parameter is often referred to as the 'impact parameter'. Most collisions will not be head-on, but somewhat displaced with respect to the opposing particle, resulting in an almond-shaped interaction area at first impact. This is illustrated in figure 2.4, where z-direction is the beam-direction, x-direction is the directions for which parts of the colliding nuclei "escaped", and y is the direction for which the long side of the almond-shape points. The resulting dynamics lead to the almond-shape flattening out in the z-direction (to something more like a bun or a macaron). This is because of the enhanced momentum component in the xz-plane, with respect to y.

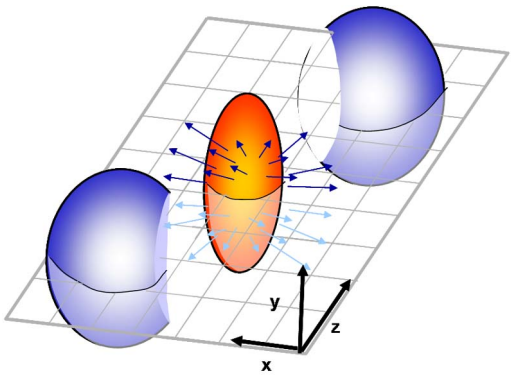

Figure 2.4: The general shape of the interaction region as two heavy nucleons collide. The reaction plane, spanned by x and z directions, is included. Beam direction is in z direction. As seen, the initial shape of the interaction region is almond-shaped [3].

The resulting hot dense ball is what is known as the QGP, an exotic state of matter, which rapidly expands and cools down. In the LHC, the QGP has a lifetime of $\sim$ 10 fm, which is about 1,2 times more than at RHIC, with volume about 300 fm^3, which is about two times larger than at RHIC. In this unconfined phase, the partons are unbound to hadrons and act as quasi-free particles. Due to internal pressure, the plasma expands and thus starts to cool down. As it cools down, in a process known as freeze-out, the energy released quickly start a hadronisation process. There are two levels of freeze-out, namely the chemical and the kinetic. In the chemical phase, the hadrons have started forming and is in a hadron gaseous form. Here, the strong interaction still acts between the hadrons due to the small distances involved. However, the quarks and gluons are no longer (quasi-) free. The thermic energy and distance between the (hadronic) particles are now low enough to regain confinement. However, there may still be hadron-hadron interactions.

As times goes on we reach the kinetic freeze-out, where the temperature and density has become low enough for the hadrons to enter into a final state hadron spectra, which

means they produce particles that can actually be detected. A kinetic freeze-out is reached when the mean distance between the interacting hadrons becomes larger than the range of the strong interaction [29].

2.2.2 Observables of the QGP

Heavy-flavor quarks are good probes for the study of the QGP, specifically the charm and beauty (c and b) quarks, as these have a formation time of 0,1 fm/c and 0,01 fm/c, respectively. They may only be produced in the initial hard scattering process of the collision, due to their large masses, which require large momentum transfers. Since the QGP forms in about 0,3 fm/c at LHC energies, these quarks can be produced in the pre-QGP phase, and experience the full evolution of the QGP [30, 31].

There are challenges to studying the properties of the QGP. This state of matter cannot be probed directly, as it is too hot and dense, and the primary particles produced within the QGP generally have such high energies that they decay before direct observation. To get to the actual observables, we need to first look into expected behaviors of produced particles as they interact with the QGP. The two main observables of interest are the *second Anisotropic Flow coefficient*, v_2, and the *Nuclear Modification factor*, R_{AA}.

Anisotropic Flow

One of the methods of studying the properties of the QGP is to look at its evolution from collision to freeze-out. The resulting final-state particles are not expected to spread out evenly. In the hypothetical case of nuclear effects, that is the coherency of nuclei, not playing a role, and the QGP not forming[3], the resulting yield of particles should be a scaling of pp-collisions. However, because of the geometric considerations of the impact area, this is not the case. Anisotropic flow is the measure of momentum anisotropy, that is, the degree to which the resulting particle momenta are asymmetric. The development of anisotropic flow depends on initial spatial geometry of the collision, as well as the transport properties and equation of state of the system [5]. The use of a Fourier series to decompose the azimuthal distribution of produced particles looks as follows:

$$\frac{dN}{d\varphi} \propto 1 + 2\sum_{n=1}^{\infty} v_n \cos[n - (\varphi - \Psi_n)]\,,$$

[3]which of course is not the case

where anisotropic flow is quantified with coefficients v_n and corresponding symmetry planes Φ_n. The first four v_n, that is v_1, v_2, v_3 and v_4, are called radial, elliptic, triangular and quadrangular flow. Of most interest is the elliptic flow (v_2), as the initial shape of the reaction volume is expected to be elliptical.

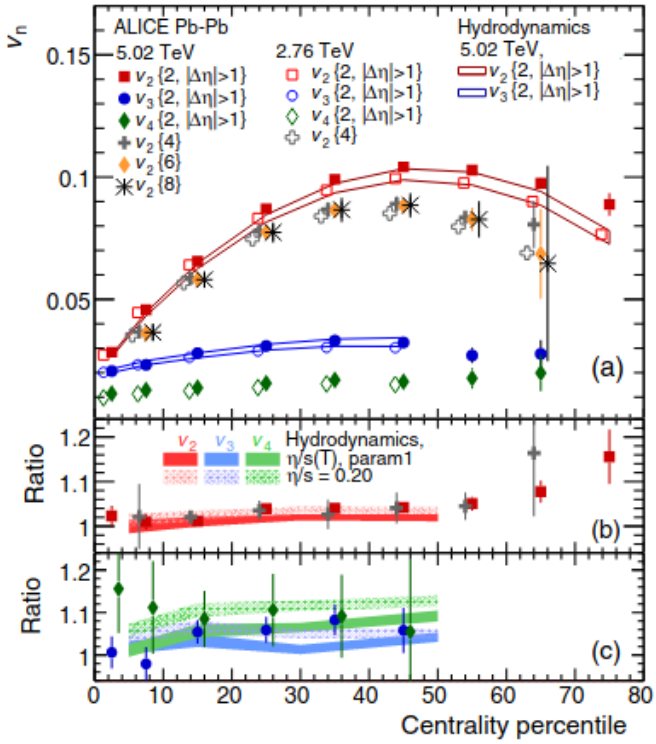

Figure 2.5: Anisotropic flow v_n integrated over the p_T range $0.2 < p_T < 5.0$ GeV/c, as a function of event centrality, for two-particle and multiparticle cumulant methods. Measurements for Pb-Pb collisions at $\sqrt{S_{NN}} = 5.02(2.76)$ TeV are shown by solid (open) markers [4]. The cumulant ratios of v_2 between Pb-Pb collisions at 5.02 and 2.76 TeV are presented in (b) and (c). Various hydro-dynamic calculations are also presented [5].

The Nuclear Modification factor R_{AA}

The topic of interest in this thesis will be the proton-proton (pp) collisions. This is of interest both as a basis for comparison with heavy-ion collisions through the nuclear modification factor R_{AA}, and for baseline studies of QCD.

As a produced hadron, or the resulting spray of particles, known as jets, transverse the volume of the QGP, strong interactions with the deconfined medium result in a modification of the output signature. Hypothetically, given no nuclear or medium effects, the differential yields, $\frac{\mathrm{d}N}{\mathrm{d}p_T}$, should scale according to the number of inelastic collisions

from a pp collision to a p-A or an A-A collision. The heavy-ion collisions would then be a superposition of independent nuclei-nuclei (NN) collisions with incoherent fragmentation. In reality, this is not the case, as there are QGP effects to consider. The exact details of these effects are still a topic of investigation, so the nuclear modification factor R_{AA} is being used as a good observable to provide information about the effect of the medium on the jets and particles. It compares the output, in terms of particles per transverse momenta, $\frac{\mathrm{d}N}{\mathrm{d}p_T}$, of proton-proton collisions with that of proton-nuclei or nuclei-nuclei collisions. The nuclear modification factor is defined as follows:

$$R_{AA} = \frac{dN_{AA}/dp_T}{\langle N_{\mathrm{coll}} \rangle dN_{pp}/dp_T},$$

where dN_{AA}/dp_T is the differential particle yield in nucleus-nucleus collisions[4], dN_{pp}/dp_T is the differential yield in proton-proton collisions and $\langle N_{\mathrm{coll}} \rangle$ is the number of binary nucleon-nucleon collisions based on the Glauber Model of nuclear interaction [32]. Since the non-scaling of these momenta-distributions comes from the nuclear and medium effects, the value of R_{AA} indicate the magnitude and direction of these effects. If $R_{AA} = 1$, this indicates no effect. For quarks, this would be a surprising find, as it would indicate that the fireball didn't strongly interact with the colored particles produced. Experimental results have however showed that this holds true for color neutral objects, such as photons, that does not interact via the strong force [33]. For $R_{AA} > 1$, that is, more yield for the heavy ion collisions than pure proton collision, the jets and particles would be enhanced by the medium. For $R_{AA} < 1$, this would indicate a suppression in the medium. For jets, this is known as quenching.

2.3 Jets

High energy partons can only be created during the hard scattering of the initial collision, during the short time period before the QGP is formed (~ 1 fm/c). Some of these partons therefore experience the whole evolution of the QGP. While the fireball is still raging (~ 10 fm/$c \cong 33$ ys[5]), these high energy partons may already start the hadronisation process. With sufficiently high energies, these hadrons can produce collimated[6] showers

[4] In the case of proton-nucleus collisions, the definition is similar, with dN_{pA}/dp_T instead of dN_{AA}/dp_T

[5] ys = yoctosecond, meaning 10^{-24} second.

[6] collimated meaning several parallel rays, made in a "column"

of partons. These showers are known as jets. In many cases, jets are observed back-to-back in the center-of-mass frame of the initial decaying particle, because of the details of the hadronisation process. This kind of jet-symmetry is known as a dijet. From each recorded event, a mapping out of the observed particle trajectories, combining both position and momentum information, can be made. Each such trajectory is known as a *particle track*. Three different event mappings can be seen in Figure 2.6, together with different interpretations of the jet structure. The left-hand one is a dijet, stemming from an $e^+e^- \rightarrow q\bar{q}$, in which there have been a soft and collinear showering followed by a transition to hadrons. The middle and right-hand ones are two different interpretations of the same event readout. The middle one is then a $q\bar{q}$ emitting a hard gluon g, followed by soft and collinear showering, and the right-hand one is a $q\bar{q}gg$ event. Deciding between these interpretations amounts to a selection of how hard and separate in angle an emision needs to be in order to be considered a separate jet. Given the vast amount of events to be considered in a data sample, in the order of millions, computers are needed to interpret the data. Thus, in order for us to instruct the computer's handling of information, we need a jet definition.

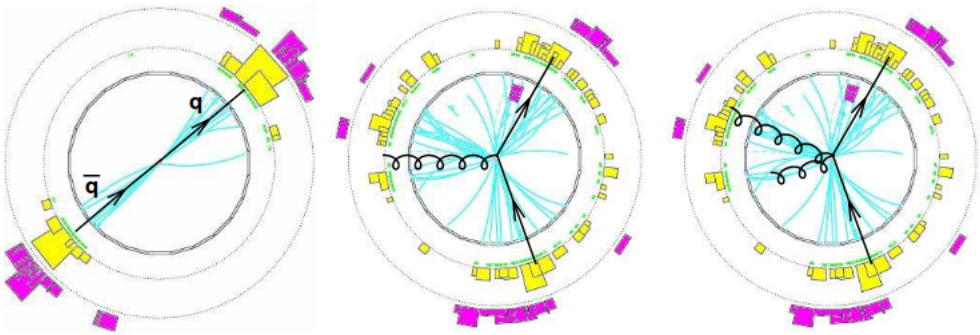

Figure 2.6: Left: an e^+e^- event that can be interpreted as having a dijet-structure, coming from a $q\bar{q}$ event. Middle: an event that can be interpreted as having a 3-jet, $q\bar{q}g$, structure. Right: the same event reinterpreted as having a 4-jet structure, $q\bar{q}gg$ [6].

2.3.1 Jet definition

A jet is a collimated collection or 'shower' of partons, that is, several particles moving in a common direction. In analysis work, defining which collection of particles should be determined as a jet is a challenge since one relies on a definition which can be interpreted both experimentally and theoretically. In both theory and experiment, results are often presented in terms of jet cross sections [6]. On the one side, there are several processes

that could theoretically take place at or near the vertex point. Four examples of possible events, leading to the same jet structure, is illustrated in Figure 2.7.

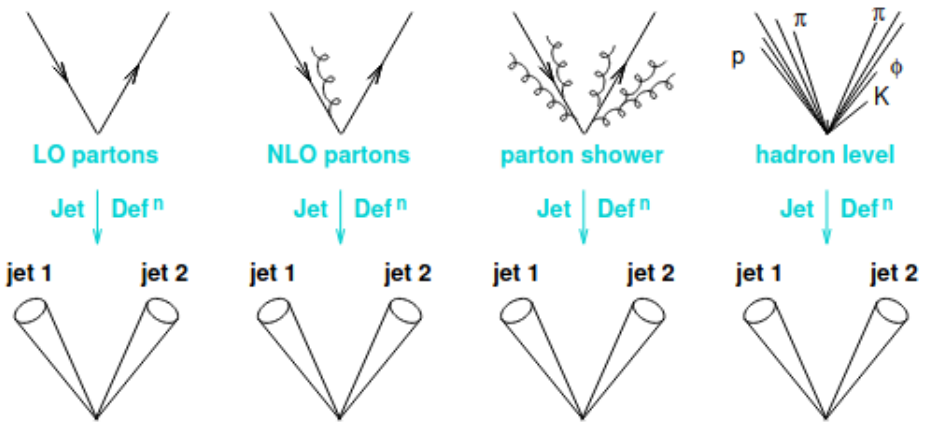

Figure 2.7: The application of a jet definition to a variety of events that differ just through soft and collinear branching, should give identical jets in all cases [6].

On the other hand, we have the (somewhat) raw data from the detectors. The methods used to determine which events produced a jet are known as recombination algorithms. In constructing a jet, there are several considerations:

- Which particles should be grouped together as a jet? The specific rules and choices for this is known as a jet algorithm. Included here are several parameters including the accepted angular reach, R, a jet could have.
- How are the momenta of the included particles to be combined? The methods used here are known as 'recombination schemes'. A common method of recombination is simply adding together all the 4-vectors of the particles. This produces massive jets, though, which can not be considered a direct representation of a parton since these are massless.

The combination of the jet algorithm, with its parameters, and the recombination scheme specify a 'jet definition'. In analysis work, a C++ package called FastJet is used for a broad range of jet finding and analysis tools [34].

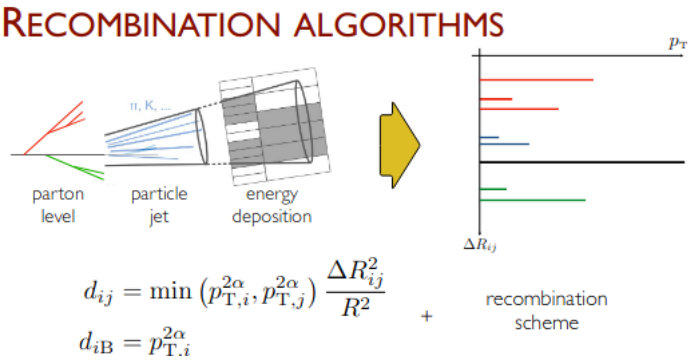

Figure 2.8: A schematic view of the recombination method for hadron jets. Each color represents a different avalanche originating from the same splitting from the original hard particle [7].

There are several known methods of recombination. In broad terms, there are two main classes of these algorithms. One can be considered a top-down approach, while the other is a bottom-up approach. They are known as cone algorithms and sequential-recombination algorithms, respectively [6]. A short overview of each method class will be described, and further detail will be provided for a specific sequential-recombination algorithm, the anti-k_t method, which is the algorithm utilized in this thesis.

Cone Algorithms

The basic idea for a cone algorithm is to find a seed particle, define a geometrically 'perfect' cone about this seed, recombine nearby particles and use this as a new seed. The initial seed is taken as the largest available p_T particle. A cone of a predetermined radius, R, is drawn around the seed, and all particle momenta within are summed up. If the direction of this sum of momenta differs from that of the original seed, the sum of momenta is taken as a new seed. One iterates this process until the sum of momenta coincides with the previous seed, i.e., with the axis of the cone. At this point, we call it a 'stable cone'. One advantage with this method, is the fact that with a stable cone, given that the QCD processes leaves the direction of a parton's energy flow essentially unchanged, such a cone very closely represents the original parton in direction and energy.

One significant weakness of the cone algorithm approach is that such algorithms are collinearly unsafe. This means that they may misidentify the appropriate leading particle, if the particle has undergone a hard splitting causing a transverse momentum loss such that its transverse momentum is less than another particle of the same jet. Then there

may be a divergent real and positive contribution to the actual jet that is not included in the reconstructed jet.

A method of collinearly safe cone reconstruction has been developed at the Tevatron accelerator at Fermilab, using all possible particles as seeds. Although this method also runs into a similar problem known as infrared-safety. Thus, a Seedless Infrared Safe Cone algorithm was developed to deal with this problem [35].

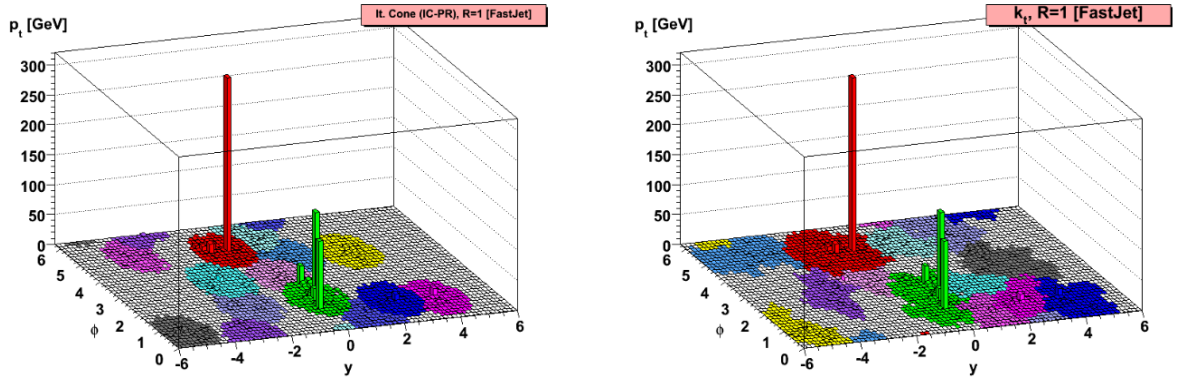

Figure 2.9: Result of a simulated test of the FastJet cone (left) and k_t (right) reconstruction algorithms. As seen, the cone method creates perfect circles, while the k_t method creates more irregular shapes [6].

Sequential-Recombination Algorithms

The sequential-recombination approach inverts the sequence, instead building the jets from the bottom up. They start by relating the distances between all pairs of particles, d_{ij}, and between such particles and the beam $d_{iB} = p_{ti}^2$. The various sequential recombination algorithms differ mainly in their particular choices of distance measure and stopping criterion. With the radius, R, playing a similar role as in the cone algorithms, the distances are found with [6, 34]

$$d_{ij} = \min(p_{ti}^2, p_{tj}^2)\frac{\Delta R_{ij}^2}{R^2}. \tag{2.5}$$

where p_{ti} is the transverse momentum of particle i with respect to beam direction (z) and $\Delta R_{ij}^2 = (y_i - y_j)^2 + (\phi_i - \phi_j)^2$. They then search for the smallest of the d_{ij} and d_{iB}, and if a d_{ij} is found, they are combined into a single particle. This particle will be called a 'pseudojet'[7]. If a d_{iB} is found, this i-th particle is then removed from the list of

[7]NB: In FastJet, PseudoJet is actually used to denote any generic object with 4-momentum

particles, and is called a jet. This process is iterated until no more particles are left. This specific example of a sequential-recombination algorithm is known as the k_t algorithm. The results of a FastJet simulation of both the cone method and the k_t method can be seen in Figure 2.9.

A development from this method is the anti-k_t algorithm. This uses a similar logic, but with the distance finding from Equation (2.5) somewhat flipped,

$$d_{ij} = \frac{1}{\max(p_{ti}^2, p_{tj}^2)} \frac{\Delta R_{ij}^2}{R^2}, \tag{2.6}$$

with $d_{iB} = \frac{1}{p_{ti}^2}$. This algorithm essentially behaves as an idealised cone algorithm, in that jets with only soft fragmentation are conical and the algorithm is both collinear and infrared safe [36]. A schematic overview of three different methods can be seen in Figure 2.10.

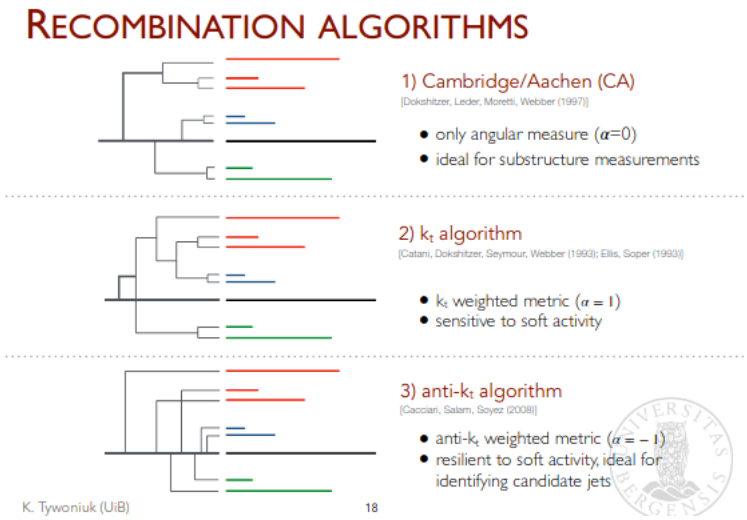

Figure 2.10: Methods of the recombination. The algorithm in 1) is similar to the k_t algorithm, however, does not rely on momentum weighting, only distance. The algorithm in 2) is the k_t method, with weighted momenta. In 3), there is the anti-k_t, with opposite weighting to the normal k_t method [7].

2.3.2 Underlying event

From high energy collisions of hadrons with hard processes, it is assumed that the resulting final state is a combination of the hard parton-parton scattering (jets) and the Underlying Event (UE). The UE constitutes the rest of the particles, which include secondary, softer processes as well as beam remnants [37]. This UE contaminates jets with a

high density of low-momentum particles, polluting any interesting hard events with many soft particles. One way of correcting for this involves the use of jet "areas" that provide a measure of a given jet's susceptibility to soft contamination. Jet areas can be determined for example by examining the clustering of a large number of additional, infinitesimally soft "ghost" particles [38]. Together with a determination of the level of UE noise in a specific event, one can then perform event-by-event and jet-by-jet subtraction of the contamination [34]. Subtraction of UE is especially important in heavy ion collisions, i.e., Pb-Pb collisions, while the UE is expected to be smaller in pp collisions.

2.3.3 Jet modification

For a jet originating in the QGP, the signature readout will not be as symmetrical as the initial hadronisation and fragmentation would indicate. Suggested first by Bjorken [39], given a jet produced in the QGP, we should see a suppression from their interaction with the hot color-charged medium. Of particular interest are the dijets produced near the edge of the QGP, as one of the jets would escape the plasma 'fireball', barely modified, while the other would transverse a large portion of the QGP and experience many interactions, thus losing more of its initial energy. The resulting readout in the detector would be one very sharp, high p_T peak on one side of the detector, and on the opposite side in the azimuthal plane, ϕ, one would see a much smaller and somewhat more smeared out peak. Such an event is referred to as a highly asymmetrical dijet. The highest jet peak is called the leading jet, and the lower, quenched peak, is called the subleading jet. The degree of quenching of the subleading jet is a good probe for the effects of the QGP on the jet-development. Quenching can be clearly seen in Figure 2.11. The summed transverse energy in both hadron and electromagnetic calorimeters are used. One challenge of correctly identifying all the subleading jet tracks, is the fact that the UE information becomes dominating below $35 - 50\,\mathrm{GeV}/c$. The relatively high limit for the subleading jet p_{T} has been chosen at 50 GeV/c, as a cut of lower than 50 GeV/c will include considerable amounts of UE information.

For a perfectly unmodified dijet signature, the height and distribution of the jet readouts should look about the same. However, as can be seen, the sub-leading jet has both a lower energy top and its p_{T} distribution appears significantly more "smeared out".

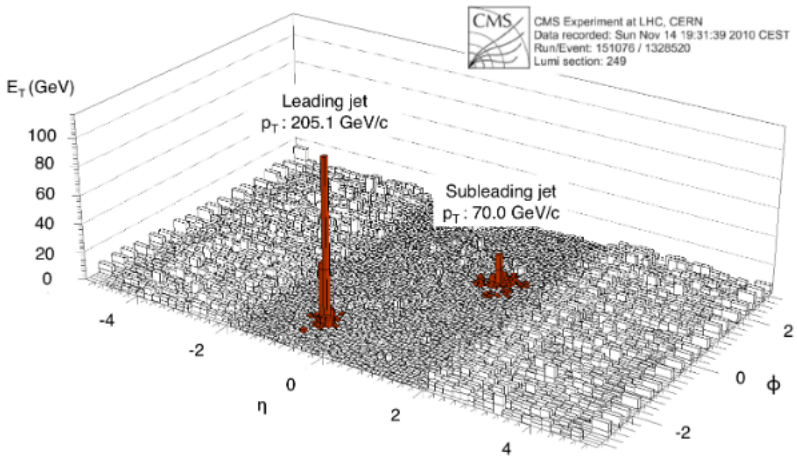

Figure 2.11: Example of an unbalanced dijet in Pb-Pb collision event at $\sqrt{S_{\mathrm{NN}}} = 2.76\,\mathrm{TeV}$. Plotted is the summed transverse energy in the electromagnetic and hadron calorimeters vs. η and ϕ, with the identified jet highlighted in red, labeled with the corrected jet transverse momentum. Figure and caption from [8].

Chapter 3

Experimental Setup

This chapter will describe A Large Ion Collider Experiment (ALICE), one of the four large experiments at the Large Hadron Collider (LHC), focusing on the sub-detectors most relevant for performing the analysis described in this thesis.

3.1 Large Hadron Collider

The Large Hadron Collider (LHC) is currently the largest and most energetic particle accelerator and collider. It is located in Geneva, under the Swiss-French border, with some of its experiments located in Geneva and some in France. It is situated about 100 meters underground, and its circumference is about 26.7 km. The LHC is currently designed to accelerate and collide protons with a center-of-mass energy of up to 14 TeV.

At the LHC there are two multipurpose detectors, ATLAS and CMS, two somewhat more specialized detectors, ALICE and LHCb, and four other smaller and very specialized detectors. Just outside the border of Geneva, in French territory, lies the ALICE detector. This experiment is built with detectors and technology to handle the massive amount of particles created in heavy ion collisions. During the creation of the QGP, thousands of particles are created, and the particle tracks need to be reconstructed and the particle species identified. The de facto setup of the different experiments along the accelerator can be seen in Figure 3.1 [9].

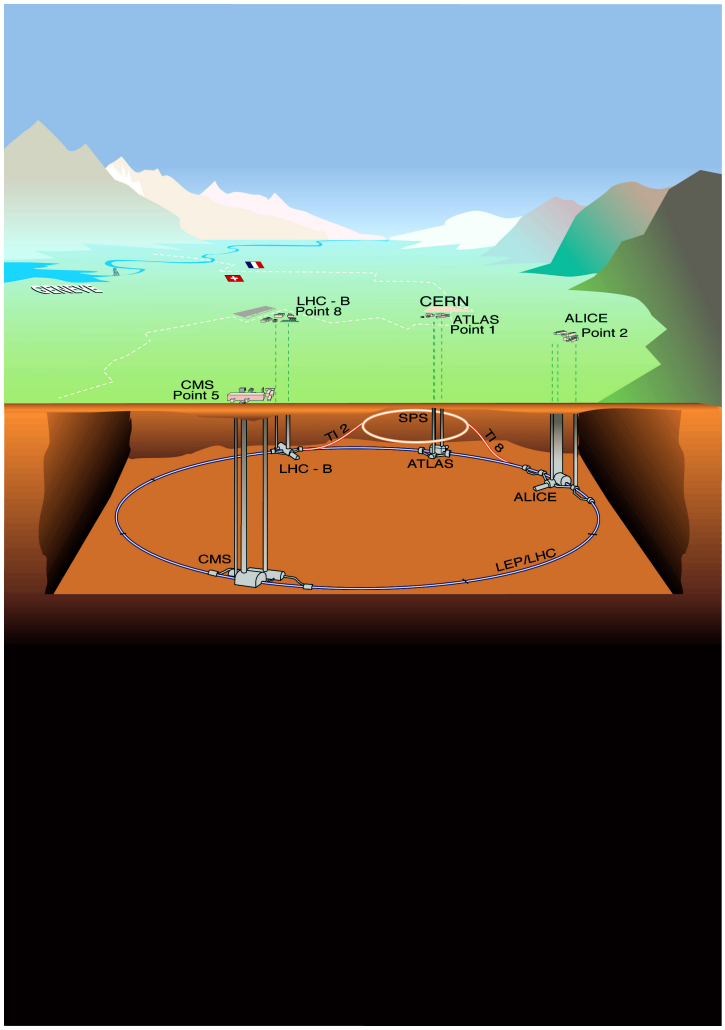

Figure 3.1: Schematic overview of the LHC accelerator, with several of its main experiments. The dashed white line indicates the border between Switzerland and France [9].

The LHC proton beam consists of several bunches of protons, with about $1,15 \cdot 10^{11}$ protons per bunch. The nominal spacing between bunches are 25 ns, with a maximum number of bunches per ring at 2808 [40].

3.2 A Large Ion Collider Experiment

At the LHC, A Large Ion Collider Experiment (ALICE) was suggested in 1993[1], green lit for development in 1997 and first used in 2010 [42], as the first dedicated heavy ion detector. The important detectors are here listed in order from innermost to outermost:

[1]The name ALICE was first suggested in a letter of intent in 1993, though the basic idea of such a experiment was suggested the year before [41].

Inner Tracking System (ITS), consisting of the Silicon Pixel Detector (SPD), the Silicon Drift Detector (SDD) and the Silicon Strip Detector (SSD), Time Projection Chamber (TPC), Transition Radiation Detector (TRD), Time Of Flight (TOF) and ElectroMagnetic CALorimeter (EMCAL). A schematic overview can be seen in Figure 3.2. The central barrel covers polar angles from 45 degrees to 135 degrees, corresponding to pseudorapidity $|\eta| < 0,9$. Covering the central barrel is the solenoid magnet with magnetic field strength $B = 0.5$ T.

ALICE was designed to be able to handle the very large particle multiplicity expected in high energy Pb-Pb-collisions. Both the ITS and the TRC are important both for tracking and Particle Identification (PID). The main detector used for PID is the TPC. Within relatively low transverse momenta (p_T between 0,15 to 2 GeV) ALICE has a good capability to identify particles, with the TOF detector providing PID in intermediate range ($\sim$ 2,5 GeV), [43] [11].

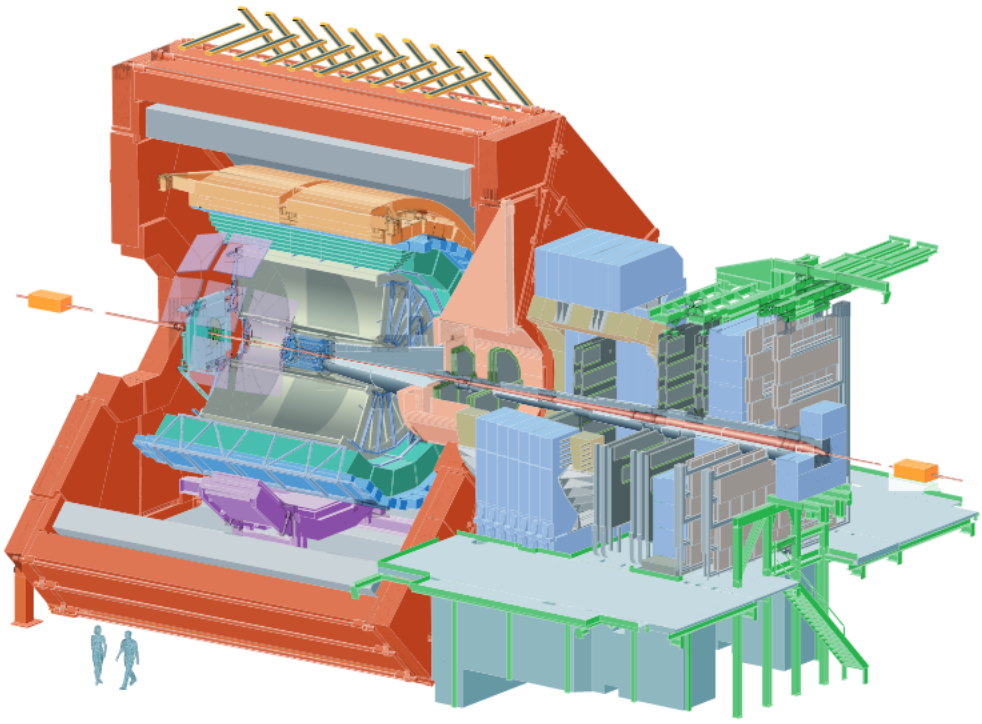

Figure 3.2: Schematic layout of the ALICE experiment, including the ITS (small blue part in the middle) and the TPC (second to inner, the "hollow" section). The red outermost layer is the solenoid magnet. On the right, we see various triggering systems. Two human silhouettes for scale [10].

At the forward end of the system, there are several smaller detectors, namely ZDC, PMD, FMD, T0 and V0. These detectors are mainly used for event characterization and

event triggering. Most relevant for this thesis is the V0 minimum bias trigger. The ITS with its subsystems, the TPC and the V0 will be described in more detail in the following subsections.

Lastly, there is the muon spectrometers, situated at angles 2-9 degrees, which is dedicated to the detection of muons.

3.2.1 Inner Tracking System (ITS)

The Inner Tracking System (ITS) is the innermost arrangement of detectors, and the first layers the product particles from the vertex point will transverse. It's main feature is tracking. It also provides Particle Identification (PID) at low p_{T} ($p_{\mathrm{T}} < 200$ MeV/c).

The ITS consists of 6 layers of silicon based detectors, with two of each of Silicon Pixel Detectors (SPD), Silicon Drift Detectors (SDD) and Silicon Strip Detectors (SSD). The inner layer of SPD has a higher pseudorapidity coverage of $|\eta| < 1.98$, to work together with the Forward Multiplicity Detectors (FMD) to provide good coverage for charged particle multiplicity. The nominal clearance from the beampipe is 5 mm. The density of particles transversing the first layer of the ITS is expected to be about 50 particles per cm^2. However, at a radius around the outermost detector of ITS, the second SSD, the densities are expected to be about one particle per cm^2. For the intermediate SDD layers, the density is expected to be about 7 particles per cm^2 [10].

SPD, SDD, and SSD are positioned on a rigid carbon-fibre structure with an accuracy of less than 100 μm. A cross section of the structure can be seen in Figure 3.3.

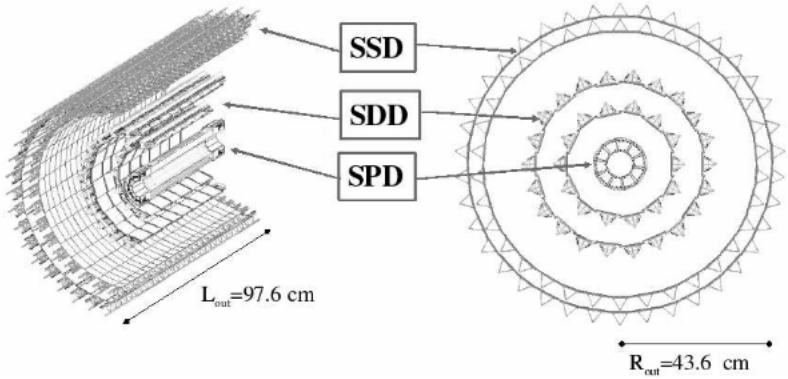

Figure 3.3: The basic structure of the ITS, with the inner layers being SPDs, the two innermost jagged layers being SDDs, and the two jagged outer layers being SSDs [10].

The four outermost layers of the ITS have an analog readout to measure the deposited charge, thereby providing a measurement of the energy loss, further referred to as $\mathrm{d}E/\mathrm{d}x$. This is mainly useful for low- p_T tracks ($p_\mathrm{T} \lesssim 0.7\,\mathrm{GeV}/c$) [11]. The energy loss used to identify particles from the ITS can be seen in Figure 3.4. The theoretical prediction for each particle species is indicated as black lines in the plot.

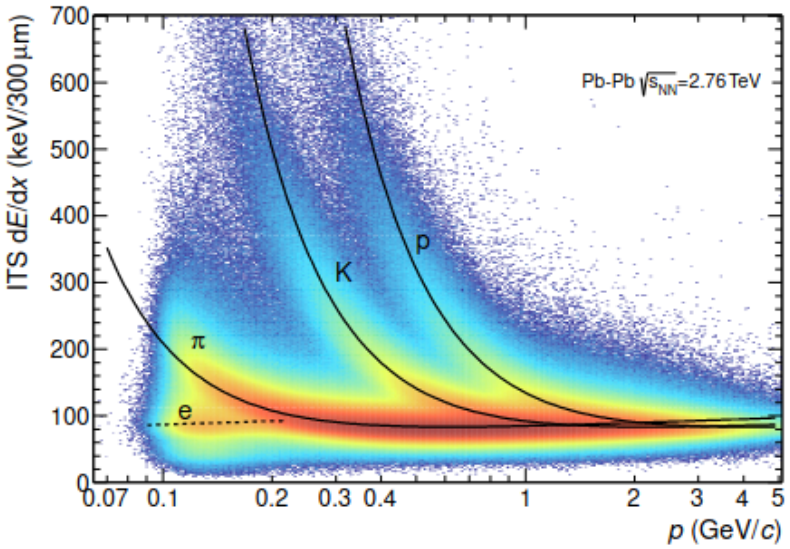

Figure 3.4: Distribution of the energy-loss signal in the ITS as a function of momentum. Both the energy loss and momentum were measured by the ITS alone. Figure and caption from [11].

Silicon Pixel Detector (SPD)

The Silicon Pixel Detector (SPD) is important for the determination of primary vertex position, as well as measurement of impact parameters to the secondary tracks created from weak decays of strange, charm, and beauty particles [10]. The SPD is structured as a matrix of 256×160 cells, measuring $50\,\mu\mathrm{m}\,(r\theta)$ by $425\,\mu\mathrm{m}\,(z)$[2]. This makes for an active area for the sensor of $12,8\,\mathrm{mm}\,(r\theta) \times 70,7\,\mathrm{mm}\,(z)$.

Silicon Drift Detector (SDD)

The Silicon Drift Detectors are the intermediate detectors of the ITS, have vary good multitrack capability, and provide two of the four needed $\mathrm{d}E/\mathrm{d}x$ samples for PID from

[2] $r\theta$ and z stated here in cylindrical coordinates

the ITS. The general idea of a Drift Chamber is to ionize the medium by the transversing charged particles, and accelerate the free electron towards a read-out wire. The electron is accelerated with sufficient energy to trigger further pairs, and an avalanche of electrons ensues. The electrons reach the wire, leading to a negative pulse on the wire.

Silicon Strip Detector (SSD)

The outer layers of the ITS consist of two layers of Silicon Strip Detectors (SSD). Their main function is measuring the position of a track, a traversing particle, in two dimensions. This is crucial in order to match tracks between the TPC and the ITS [10]. They also provide additional $\mathrm{d}E/\mathrm{d}x$ information for assistance of low momenta PID.

The SSD is constructed on "ladders", one module wide, with up to 25 modules along the beam direction. With 72 ladders, this subsystem contains a total of 1698 modules.

3.2.2 Time Projection Chamber (TPC)

The Time Projection Chamber (TPC) is the main detector of the central barrel and covers $|\eta| < 0.9$, with a reduced track length and momentum resolution coverage of up to about $|\eta| = 1.5$. The TPC is optimized for ideal two track separation, particle identification and momentum resolution. It covers the full range of azimuth angles, with exception of some regular dead zones from the geometric design of the barrel. The dead zones cover about 10% of the azimuthal. For high transverse momenta, a combined track finding with ITS and in certain cases TRD is also used. The TPC has good momentum resolution from a low p_{T} of about 0.1 Gev/c to a high p_{T} of about 100 GeV/c. The detector was designed to handle high particle multiplicities, with the expected[3] number of tracks per event being 20'000 throughout the detector volume per event.

The detector is a large gaseous detector with a radius perpendicular from the beam axis at 85-247 cm, and a cylinder length along the beam axis of 500 cm. The inner and outer radii are chosen for optimalization, by the lower limit of hit density for the inner side, while the length to the outer end is determined by the requirement to have a $\mathrm{d}E\mathrm{d}x$ resolution of 5-7% . A schematic view of the TPC detector can be seen in Figure 3.5.

The cylindrical cage is filled with $88\,\mathrm{m}^2$ of $\mathrm{Ne/CO_2}$ (90%/10%), with the main principle behind the cage being that of a drift chamber. In short, a drift chamber utilizes

[3] at the time of design.

precise measurements of the wire currents at two different points on the particles' trajectory to infer their position and speed. The gas in the chamber gets ionized, and an avalanche gets accelerated within an electric field, which reads out as a signal while the charged particle of interest passes the readout wires. The readout is done by Multi-Wire Proportional Chambers, with cathode pads mounted into 18 trapezoidal sectors of each end-plate. [12] With knowledge of both the energy loss from ionization, as well as acceleration by the internal electric field, both the position and the speed of the particle can be deduced.

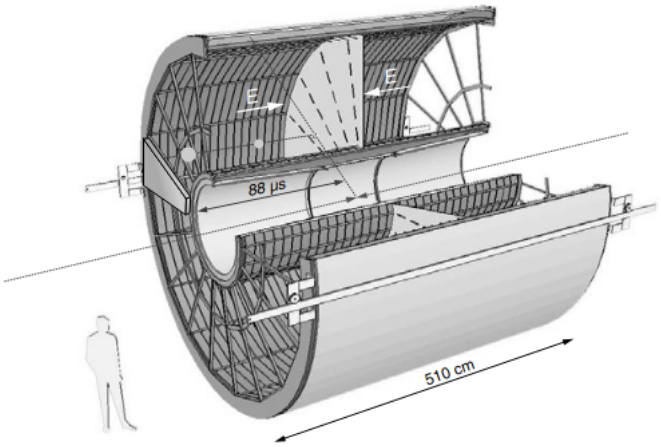

Figure 3.5: Schematic layout of the TPC. One human silhouette for scale [12].

The TPC is the main tracking detector of ALICE. In addition to tracking, the TPC also provides PID at a large variance of p_{T}. The largest separation is achieved at low p_{T} ($p_{\mathrm{T}} \lesssim 0.7\mathrm{GeV}/c$), but a good separation is also available up to $20\,\mathrm{GeV}/c$ [11]. Particle identification is performed by simultaneously measuring the specific energy loss ($\mathrm{d}E/\mathrm{d}x$), charge, and momentum of each particle traversing the detector gas. The energy loss used to identify particles from the TPC can be seen in Figure 3.6. The theoretical prediction for each particle species is indicated as black lines in the plot.

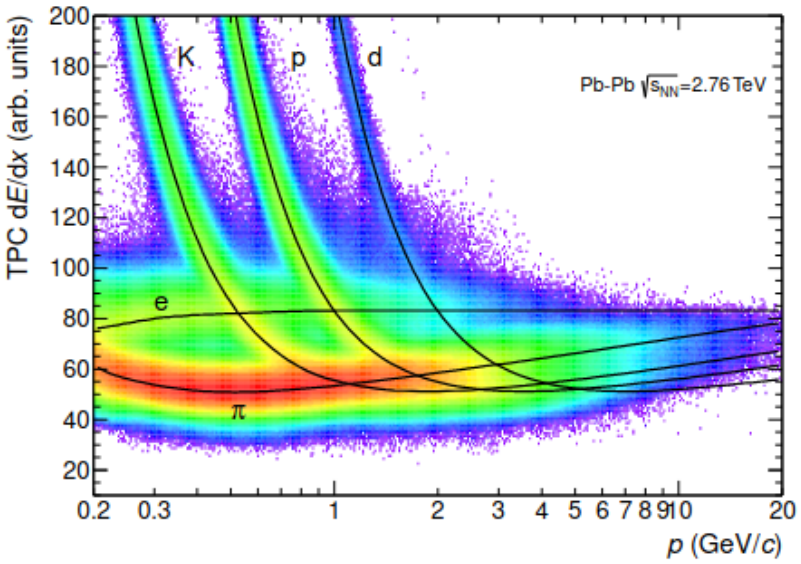

Figure 3.6: Specific energy loss (dE/dx) in the TPC vs. particle momentum in Pb–Pb collisions at $\sqrt{s_{NN}} = 2.76\,\text{TeV}$. The lines show the parametrizations of the expected mean energy loss. Figure and caption from [11].

3.2.3 Transition Radiation Detector (TRD)

The main purpose of the Transition Radiation Detector (TRD) is primarily designed for electron identification in the central barrel for momenta over 1 GeV/c [10]. It covers pseudorapidities of $|\eta| < 0.84$ and consists of 540 modules arranged in 18 sectors in the azimuth, in various sizes from 91×122 cm^2 to 133×145 cm^2. Each sector consists of 5 stacks in longitudinal direction, with 6 module layers per stack. A schematic view of the TRD detector can be seen in Figure 3.7. Here, one sector is pulled out to the second stack, with one module separated for indication.

The TRD is part of the Level 1 trigger system, and provides, among other things, recordings of J/ψ and jets. The design parameters is chosen for good pion rejection capability above 1 GeV/c, good position resolution ($\sigma_y \lesssim 400\,\mu$m and $\sigma_\phi \lesssim 1°$) and momentum stand-alone resolution of around $\frac{\delta p_\text{T}}{p_\text{T}} \approx 2.5$ - 3% for momenta below 2 GeV/c. Together with tracking in the central barrel, overall momentum resolution of better than 5% can be obtained for momenta up to about 100 GeV/c.

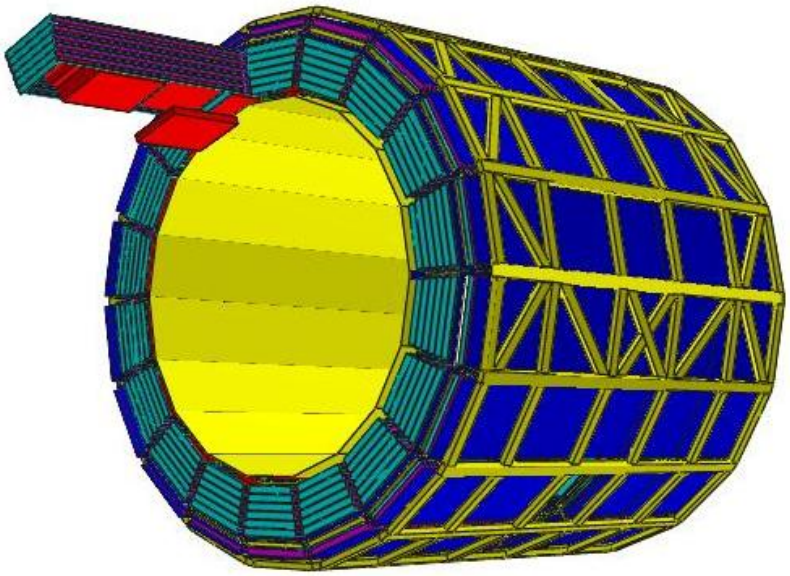

Figure 3.7: Schematic layout of the TRD, with the red section pulled out for inspection. Each of the 18 sectors can be seen evenly distributed around the azimuth. Figure from [13].

3.2.4 The V0 system

The V0 detector (often called VZERO) is used both for triggering, as well as measuring centrality. It is also a powerful tool for rejection of beam-induced backgrounds and measurement of LHC luminosity. It has two parts, the V0A and V0C, placed asymmetrically about the impact point. The V0A is situated at about 3,3 m in the forward direction, and V0C is situated about 0,9 m in the backwards direction. With this, they cover pseudorapidities of $2.8 < |\eta| < 5.1$ and $-3.7 < |\eta| < -1.7$, respectively. [44] The V0 functions as a level 0 (L0) Minimum Bias (MB) trigger. L0 is one of three levels of triggers that are all sent to the Central Trigger Processor, which together with the LHC clock and timing synchronization information, distributes trigger information to the whole ALICE experiment.

Minimum Bias: MB trigger uses a combination of the trigger from V0A, V0C and SPD, requiring at least two of the following three conditions to be satisfied:

- At least two pixel chips hit in the outer layer of SPD
- A signal in V0A
- A signal in V0C

This means that at least one of the V0-sides are triggered, or both if there are no double pixel hits in SPD.

3.2.5 Pileup

In pp collisions, a phenomenon known as 'pileup' occurs. For each bunch-crossing, the interesting events are those of high energy (hard) collisions. Pileup is a result of additional soft pp collisions, where at each bunch crossing there will be of the order of 20-25 additional minimum bias pp interactions. These additional collisions pollute the final state of the interesting hard collision. There are two main categories of pileup. In some cases, the bunch-crossing can have two or more collisions occurring for the same bunch-crossing. This is known as in-bunch pileup. In other cases, the pileup is a result of collisions that occurred in a different bunch crossing than the one which triggered the acquisition [45]. These pileup-events, known as out-of-bunch pileup, are still present in the detector due to the slow readout time of the detectors like TPC. Both of these types of pileup must be taken into consideration during an analysis, and will be further discussed in Section 4.3.

Chapter 4

Analysis

The analysis in this thesis will look at charged jets in data recorded by ALICE at the LHC. Data from data taking run 2 is used, recorded during 2017 (LHC17) and 2018 (LHC18). The measured, raw jet p_{T} spectra is extracted. The measured spectra are then unfolded to take into account the error from recording limitations, such as diffusion and detector acceptance. The jet p_{T} spectra are extracted using an analysis framework developed for the analysis of J/ψ mesons decaying into leptons, as a case study for the future analysis of J/ψ tagged jets. It is important to make sure that the implemented structure for jet finding is working robustly. Two different trigger conditions will be compared, namely Minimum Bias (MB) triggered events and Transition Radiation Detector (TRD) triggered events.

The analysis presented in this thesis provides the groundwork for further studies of heavy flavor tagged jets, especially configured for the search for J/ψ candidates in jets.

4.1 Analysis software

This analysis is performed using the ALICE analysis framework, namely the packages AliRoot [46] and AliPhysics [47]. Both packages utilize ROOT [48], an object-oriented programming framework using the C++ programming language. The AliRoot package is used for processing of raw data and Monte Carlo (MC) simulations. The PYTHIA program is a tool used for generation of high-energy collisions using MC simulations to reduce complex final states to the initial hard processes [49]. The GEANT4 simulation

toolkit is used for simulating particle passage through the detector material [50]. Events generated in this way then deposit their energies in the simulated detector, which is transformed into real detector responses, including any possible electronic signal manipulation. The reconstruction procedure, as described in Section 2.3.1, is the same for both raw data processing and MC generated event simulations.

The output of the reconstructed event is in the form of an Event Summary Data (ESD) file, which for MC also includes the full information about the generated particles, namely the particle species and momentum. The ESD files contain complete information describing the events, and are thus very large. To get the data in a more user friendly form, a set of refilterings is done on the ESD, and this reduces the data information to a subset of information that has been selected for physics analysis, producing an Analysis Object Data file (AOD) [51, 45]. These files contain various 'passes', that must be applied when running analyses, through choosing a filterbit. This filterbit choice is necessary to avoid double counting of tracks.

The AliPhysics package includes software tools used for the analysis of real and simulated data. To access ALICE specific simulation or analysis data, event handlers are used for ESD and MC files. The analysis presented in this thesis is performed on data generated from reconstructed AOD files using the reduced tree framework found in AliPhysics/PWGDQ/reducedTree. The reduced tree framework is a framework which makes it possible to skim large data samples in an analysis specific way, producing small ROOT trees which can be further analyzed on a local computer. Several analysis tools are implemented to process and analyze the skimmed data sets. The base class of the reduced tree framework is AliAnalysisTaskReducedTreeMaker which is used to produce skimmed data. The settings for generating trees in this analysis are provided in `\AddTask_slovaas_dst_jets.C"`. The skimmed data is further processed using the AliAnalysisTaskJpsi2eeJets task, which implements the jet reconstruction.

The setup of the analysis task is determined from the macro `"AddTask_slovaas_jpsi2ee_jets.C"`, that defines all analysis cuts and creation of relevant histograms.

4.2 Data sample and MC simulation

4.2.1 Data sample

The analysis presented in this thesis is done using the Run 2 proton-proton (pp) data set recorded by ALICE at the LHC at $\sqrt{s} = 13$ TeV. The analyzed data set was

recorded between 2017 and 2018. The analyzed pp events are divided into several periods named LHC17[h-r] and LHC18[b-p][1], corresponding to data sets taken in 2017 and 2018, respectively. A period consists of one or more runs, where a run is a continuous interval of data gathering, such that each run has a consistent set of conditions. For a complete list of runs, see Appendix A. Analyzed events are triggered by the ALICE MB (Minimum Bias) trigger and amount to about 12 million events, which is about 1% of the total events in the data set. The Run2 MB trigger requires the coincidence between V0A and V0C. This is often referred to as a V0AND trigger and sometimes, as in the trigger selection codes, as INT7 (kINT7 for trigger bit 1). In addition to the MB triggered data sample, a TRD triggered data sample is analyzed. TRD triggered runs are selected with the requirement of TRD as a trigger detector and SPD, TPC and TRD as readout detectors. The TRD triggered data sample is a sub sample of the MB sample and consists of about 1.7 million events. For this analysis, pass 2 reconstruction is used for all periods.

4.2.2 Monte Carlo production

In addition to the analyzed data sample, a PYTHIA generated event simulation is used. All data taking conditions are reproduced in this simulation, including incomplete TPC sectors.
The MC production used in this analysis is anchored to pp events at $\sqrt{s} = 13$ TeV, using pass 2 reconstruction. The MC simulation consists of minimum bias events with injected J/ψ signals in the barrel. The injected J/ψ signals are added as 70% prompt J/ψ and 30% non-prompt J/ψ. For this analysis, only events with non-prompt injected J/ψ mesons are used, as the non-prompt production of J/ψ mesons is more likely to be connected with jet production. A standard jet analysis would benefit from using a jet-injected MC sample, which would give better statistics for the detector response matrix further described in Section 4.7.1. In total, about 93.7 million events in the MC sample are analyzed, where only the (approximately 30%) non-prompt J/ψ injected events are considered for further analysis. The reason for using an MC production of this type is to enable further study on the same data sampling focused on finding J/ψ candidates in jets.

[1]Explicitly: For 2017, the used periods are LHC17h, LHC17i, LHC17k, LHC17l, LHC17m, LHC17o and LHC17r. For 2018, the used periods are LHC18b, LHC18d, LHC18e, LHC18f, LHC18g, LHC18h, LHC18k, LHC18l, LHC18m, LHC18o and LHC18p

4.3 Event selection

This analysis is performed using a skimmed data set, which selects events with at least two electron candidates. In addition, the skimmed data stores so-called unbiased events consisting of 1% of the total events without any requirement for electron candidates. For the analysis of the jet spectra, only these unbiased events are considered with the following event criteria. Only pp events with good collision candidates are included in this analysis, i.e., events where a beam crossing took place. All events must pass the physics selection, ensuring good collision candidates. In addition, events are required to have a reconstructed vertex with at least one vertex contributor and $|z_{\mathrm{vtx}}| < 10$ cm. The positions of events along the beam axis is shown in Figure 4.1.

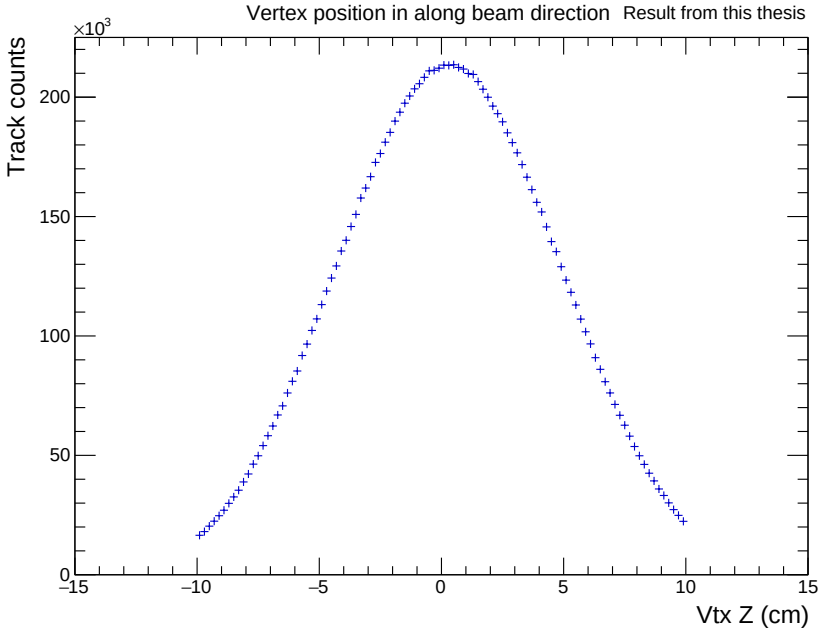

Figure 4.1: The z-vertex distribution for the total data set of both LHC17 and LHC18, after cuts have been applied. As can be seen, no events over or under 10 cm away from the principle mid-point of the beam crossing have been included.

As mentioned in Section 3.2.5, pileup effects must be taken into consideration during analysis. Two different algorithms are applied to reject in-bunch pileup events, namely SPD pileup rejection and Multi-vertexer rejection. The SPD pileup rejection is based solely on SPD information and rejects events with multiple vertices reconstructed from at least three vertex contributors each. The multi-vertexer rejects events with at least five vertices based on the full track information.

Due to the long readout time of the TPC, out-of-bunch pileup, may still be present in the selected events. One method for pileup rejection is the requirement of the particle tracks to have a given distance of closest approach. The beams at LHC will have a longitudinal spread, and it may be possible to experimentally associate each charged particle with a distinct primary vertex corresponding to a single pp interaction and subsequently eliminate some fraction of the soft contamination [52]. This contamination must be removed using track selections further described in Section 4.4.2. In total, 12 million MB triggered and 1.7 million TRD triggered events are selected for analysis.

4.4 Track selection

This analysis relies on a two part track selection, and is made using so-called hybrid tracks. Since some parts of the SPD were switched off during many run periods, inefficient regions for common track reconstruction are apparent. Hybrid tracks are used to increase the track reconstruction efficiency and ensure a uniform distribution in the (η, φ) plane. The hybrid tracks include so-called 'good global' tracks and 'constrained tracks'. The good global tracks are tracks with at least one SPD hit, and that are required to have an ITS refit, which makes sure it is constrained to the primary vertex. Constrained tracks are without SPD hits, but also with an ITS refit requirement. The tracks are selected using AOD filter bits 8 and 9 for global and constrained tracks, respectively. A definition of AOD filter bits can be found in CERN's TWiki web page for "AddTaskInfoAOD147" [53]. Hybrid tracks are required to be within the kinematic acceptance of $\eta < 0.9$ and have $p_{\mathrm{T}} > 0.15$ GeV/c. A summary of the jet track requirements can be found in Table 4.1. Figure 4.2 shows the φ distribution the hybrid track selection separated into global and constrained tracks for the total of all used periods from the 2017 and 2018 data sets. In both data sets the global track distributions show several regions with lower track counts while the constrained tracks show increased counts in these regions. Thus, the inclusion of constrained tracks ensures a flat distribution with phi, as is seen in the sum of the distributions.

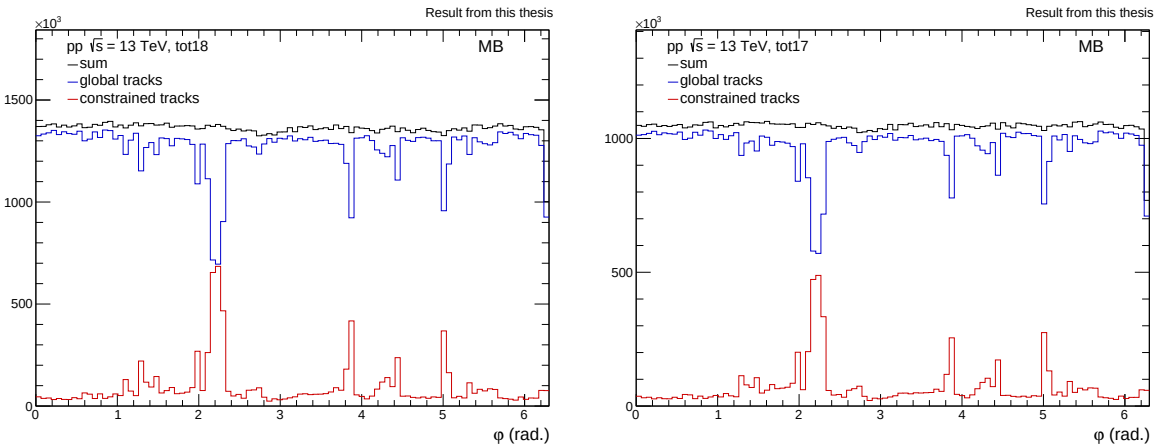

Figure 4.2: φ distribution of hybrid track selection (black) containing global (blue) and constrained (red) tracks for MB triggered events, total of (used) periods for 2018 and 2017 runs in the left and right panels, respectively.

Table 4.1: Jet track selection for global and constrained tracks, including the kinematic cuts and track quality cuts, to be discussed in the next section.

Parameters	value	comment
kinematic cuts		
$\lvert\eta\rvert$	< 0.9	
p_{T}	> 0.15 GeV/c	
track quality cuts		
TPC N_{rows}	> 70	
TPC rows/cls.	> 0.8	
TPC $\lvert\chi^2\rvert$	< 4.0	
ITS $\lvert\chi^2\rvert$	< 36.0	
require TPC refit	yes	
require ITS refit	yes	
reject kinks	yes	
$\lvert\mathrm{DCA}_{xy}\rvert$	< 2.4 cm	
$\lvert\mathrm{DCA}_{z}\rvert$	< 3.2 cm	
DCA to vertex 2D	yes	
require sigma to vertex	no	
TPC $\lvert\chi^2\rvert_{\mathrm{constr.\ global}}$	<36	bit 8
TPC $N_{\mathrm{cls.\ shared}}$	<0.4	bit 8
require SPD hit	yes	Global tracks (bit 8)
require SPD hit	no	Constrained tracks (bit 9)

The following sections describe the track selections in detail.

4.4.1 Kinematic cuts

A kinematic cut selection is applied in order to ensure that the tracks are within the acceptance of the central barrel. Tracks are required to be within geometric acceptance of $|\eta| < 0.9$, and the minimum transverse momentum required is $p_{\mathrm{T}} > 0.15\mathrm{GeV}/c$. A hit map showing the recorded jet track distribution before and after cuts can be seen in Figure 4.3 for the MB trigger and in Figure 4.4 for the TRD trigger. For MB, the track distribution is fairly uniform in the η-direction both before and after cuts. After cuts, there is a great degree of uniformity overall. The slight dip in the distribution around $\eta = 0$ is caused by the central electrode of the TPC.

The MB has significantly more uniform distribution of tracks than the TRD, even before cuts, given that the sectors and stacks of the TRD are clearly visible. The TRD hit maps serves to clearly indicate the inefficiency regions of the TRD detector. The squares visible in this hit map are due to the geometric setup of the TRD as described in Section 3.2.3. In both cases, the cuts can be seen to result in a more uniform jet track distribution.

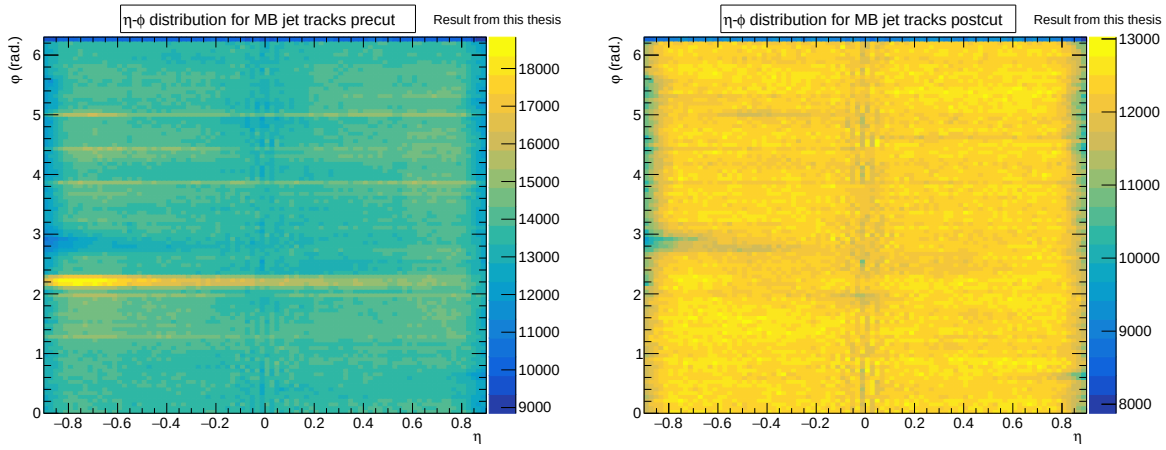

Figure 4.3: $\eta - \phi$ distribution map for MB jet tracks before (left) and after (right) cuts. The color scales of the two hit maps are different, since the maximum track intensity in both cases are shown as the brightest yellow spots. We thus see a much higher degree of uniformity in track distribution after cuts.

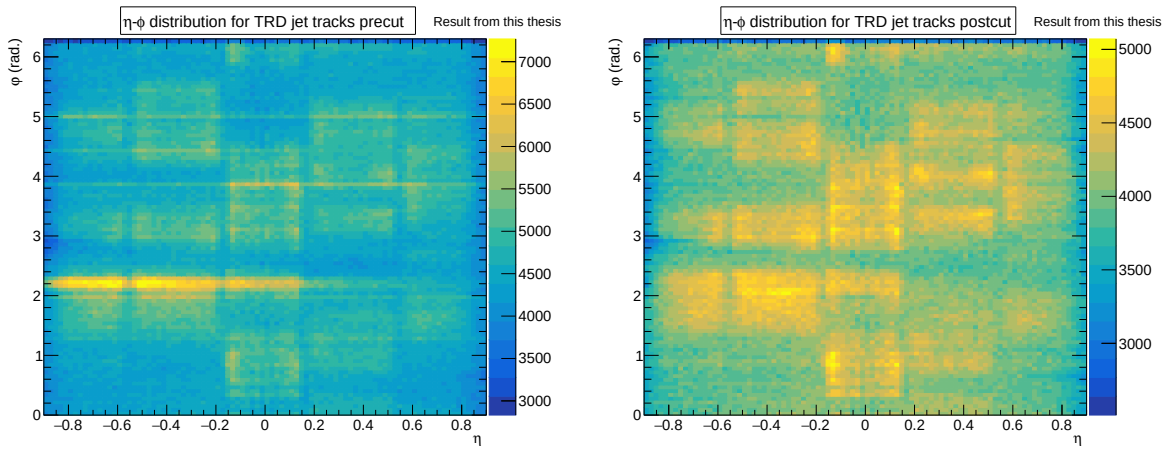

Figure 4.4: $\eta - \phi$ distribution map for jet tracks before (left) and after (right) cuts. The color scales of the two hit maps are different, since the maximum track intensity in both cases are shown as the brightest yellow spots. We thus see a much higher degree of uniformity in track distribution after cuts.

4.4.2 Track quality cuts

Several cuts are applied to ensure a good tracking quality and to reject tracks from secondary particles, background sources and pileup. A cut on the Distance of Closest Approach (DCA) is applied in the transverse plane (DCA_{xy}) and along the beam pipe direction (DCA_z), to distinguish and reduce the number of secondary vertices [54]. This cut removes secondary particles from material interactions or weak decays with larger displacements from the primary vertex. In addition, a cut on the DCA along the beam pipe reduces the number of tracks from out-of-bunch pileup, as mentioned in Section 3.2.5. Cuts of $\mathrm{DCA}_{xy} < 1\,\mathrm{cm}$ and $\mathrm{DCA}_z < 3\,\mathrm{cm}$ are applied.

Good global tracks are required to have at least one hit in the SPD, while this requirement is removed for the constrained tracks, thus recovering information from some of the missing SPD regions. The track quality is further improved by requiring ITS and TPC refit, ensuring tracks have hits in the ITS and that ITS track segments are matched to those in the TPC. TPC tracks are required to have at least 70 clusters out of 159 possible clusters. The track reconstruction is required to have a maximum $|\chi^2|$ of 4 and 36 for TPC and ITS tracks, respectively. The value is kept very loose for ITS tracks due to the small number of tracking points. Tracks associated with particle decays can be removed by rejecting kinked tracks, as the decay of charged particles into charged decay products result in the abrupt bending of tracks, known as kinks.

4.5 Jet Reconstruction

In this analysis, the jet reconstruction is done using the FASTJET [34] package. The jet clustering is performed using the anti-k_{T}-algorithm (see Section 2.3.1) incorporated in FASTJET, which is both infrared-safe and collinear-safe, i.e. not sensitive to low energy radiations or the collinear splitting of particles. The resolution parameter is set to $R = 0.4$ and the p_{T}-scheme is used for recombination. A uniform background of extremely soft massless 'ghost' particles is included in the jet clustering. These extremely soft ghost particles do not affect the set of hard particles ending up in a jet. The jet clustering takes as input the four-momentum of all jet tracks passing the track selection in Section 4.4 and returns an array of jets. Only jets passing the jet selection criteria are considered for the jet spectrum.

In this analysis, only charged tracks are used for jet reconstruction, and the underlying event is not subtracted. Reconstructed jets are restricted to have a minimum $p_{\mathrm{T}} = 10$ GeV/c and $|\eta_{\mathrm{jet}}| < 0.9 - R$ corresponding to jets fully contained within kinematic acceptance. A requirement that the jet should have a leading track of at least 5 GeV/c is also applied. The jet definition is summarized in Table 4.2.

FastJet package	v3.2.1
Reconstruction algorithm	anti-k_{T}
Recombination scheme	p_{T}-scheme
Cone radius R	0.4
Ghost area units	0.005
Ghost area type	active_area_explicit_ghosts
Jet p_{T}	> 10 GeV/c
Leading jet track p_{T}	> 5 GeV/c
$\lvert\eta_{\mathrm{jet}}\rvert$	$< 0.9 - R$

Table 4.2: Jet definition

4.6 Raw Jet Spectrum

In this section, the raw jet spectra for the different trigger modes MB and TRD will be determined. In Figure 4.5, the inclusive raw jet spectra reconstructed using the anti-k_T clustering algorithm is shown for the MB trigger readout, with parameteres described in Table 4.2. Before plotting, the raw jet p_{T} data has been rebinned into a set of 17 bins. Explicitly, each p_{T} bin boundary is set at:

[0., 10., 12., 14., 16., 18., 20., 25., 30., 40., 50., 60., 70., 80., 90., 100., 150.] GeV/c

To produce the appropriate jet spectra, $dN/dp_T d\eta$, the content of each bin has been scaled to the width of each binning[2]. The resulting content should then also be scaled to the η differential. However, as seen in Table 4.2, with cone radius at 0.4 and jets required to be fully within the $|\eta_{jet}| < 0.9 - R = 0.5$, this will give $d\eta = 0.5 - (-0.5) = 1$. We would devide by 1, and therefore - in *this specific thesis*, given the chosen parameters - this step is redundant.

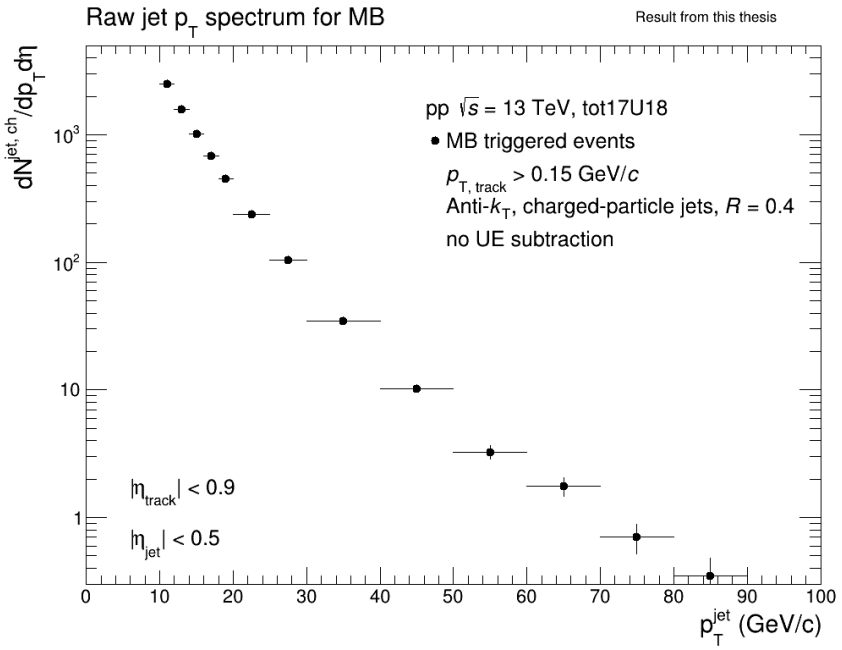

Figure 4.5: Raw Jet p_{T} spectrum for LHC17 and LHC18, total of all periods used in this thesis, taken from the MB triggered events. The spectrum is plotted with a logarithmic scale for the yield.

In Figure 4.6, both the MB and TRD triggered jet spectra are shown, with rebinning and scaling as described for MB. As can be seen, the TRD trigger has recorded more jets than the MB trigger. The TRD triggered spectrum also extends to a significantly higher p_{T}.

[2]otherwise, each bin would just show a total count of the jet tracks within each bin, and therefore the y-value would be somewhat arbitrary.

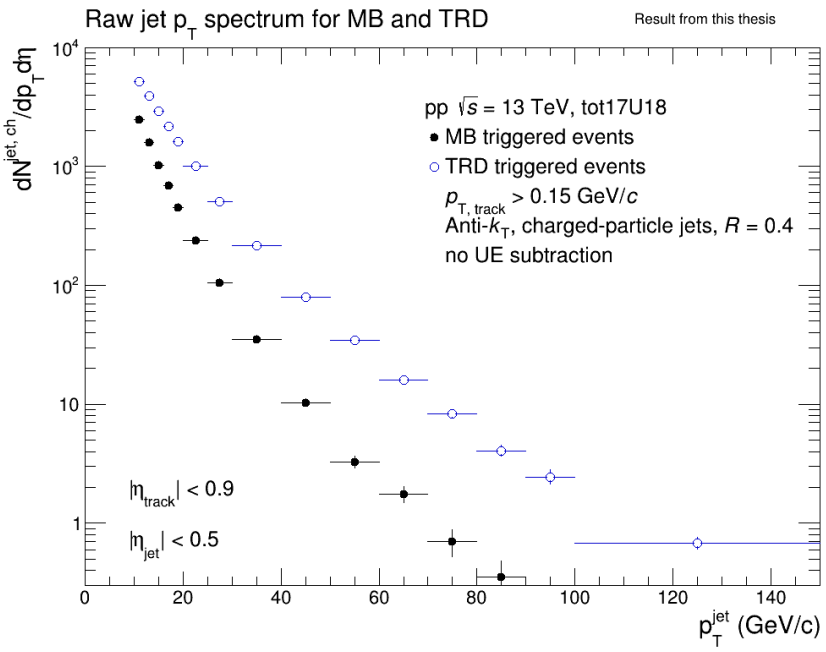

Figure 4.6: Raw jet spectra for MB (black) and TRD (blue) triggered events in the total LHC17 and LHC18 data sample. The spectra are plotted with a logarithmic scale for the yields.

The difference in the raw jet p_{T} spectrum between TRD and MB triggers can be seen in Figure 4.7. Here, for each bin, the number of MB measured jets are simply subtracted from the number of TRD measured jets.

It is important to notice that this comparison is made between jet *yields* as a function of p_{T} and not jet *cross sections*, so no normalization and trigger bias is taken into account. It can be seen that the relative difference between the spectra increases with higher p_{T}.

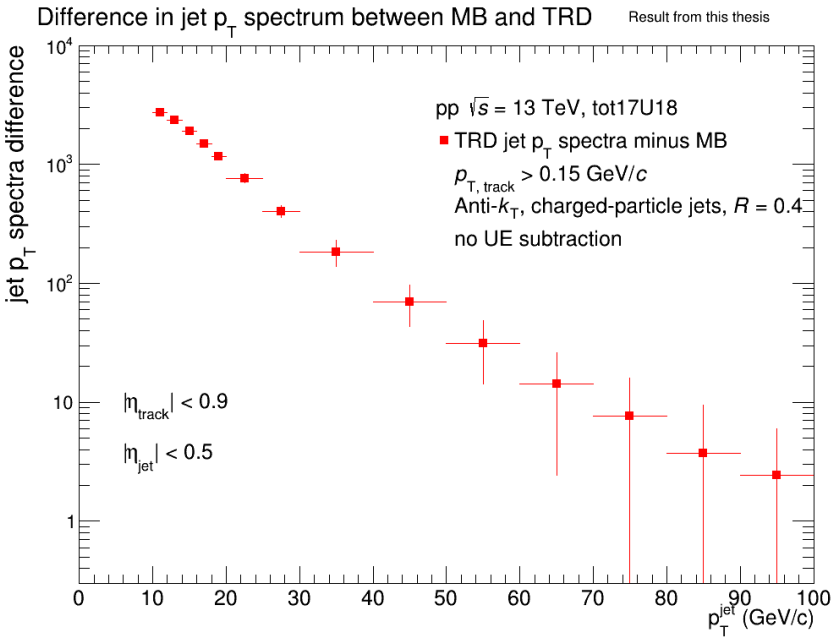

Figure 4.7: Difference in number of counts from the compared MB and TRD jet spectra shown in Figure 4.6. The spectra difference is plotted with a logarithmic scale for the yields.

The ratio of TRD triggered jet events to MB triggered jet events can be seen in Figure 4.8. The growing ratio means that there is a hardening of the TRD triggered spectrum with respect to the MB triggered spectrum.

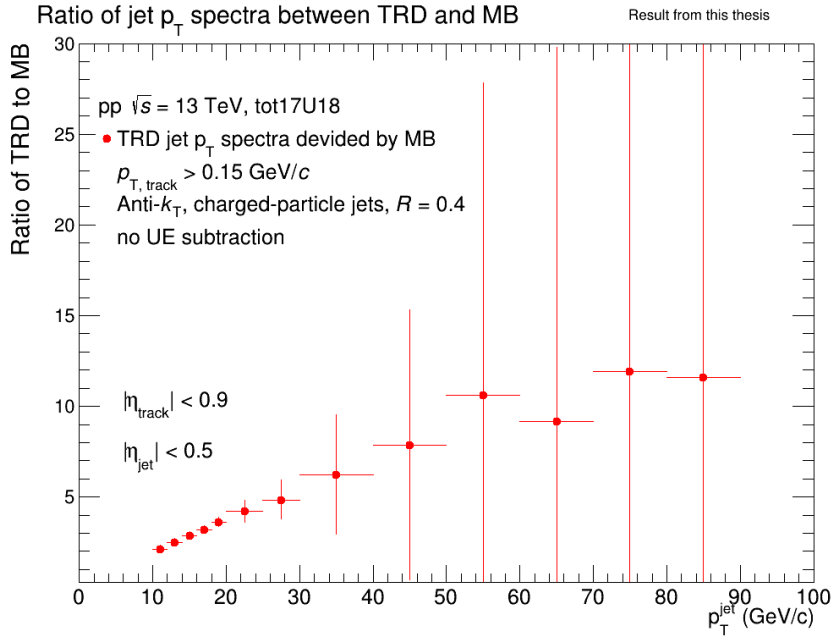

Figure 4.8: Ratio comparison of TRD over MB jet spectra.

4.7 Unfolding

The measured jet spectra need to be corrected, as some distortion from detector effects are to be expected. This distortion can come from both tracking inefficiency and detector acceptance. We correct the detector effects through a method known as unfolding. In this thesis, the iterative Bayesian method from the RooUnfold software package [55] is used.

In the unfolding process, the difference in detector level readout compared to particle level truth[3] is accounted for. The unfolding method takes as input a response matrix, a prior and the measured spectrum, and returns an unfolded spectrum. The prior should be a realistic spectrum, and for this analysis the generator level spectrum from MC is used. In this analysis, the Bayesian method with four iterations is used.

To get a better idea for the necessity of unfolding, a comparison between the MC generator level jet spectrum ("truth spectrum") and the MC reconstructed jet spectrum has been made, and can be seen in Figure 4.9. Here, the simulated 'MC reconstructed' is in principle containing a representation of what the detectors would record, given the simulated MC truth spectrum input. Thus, given a "perfect" detector response, the two spectra would have been identical. As the detector does not record the full event, an unfolding procedure is required on the reconstructed spectrum for the spectrum to represent the actual event. Another way of presenting this is shown in the plot on the right. Here, the ratio between the generator level reconstructed spectrum and the MC truth spectrum is shown. Given a perfect detector response, this comparison would give one for all p_{T} bins. In the lower p_{T} range, the ratio shows that there is a better response in the detector for softer jets, however, it trails off at higher p_{T}, loosing more and more information. As can clearly be seen, the reconstructed spectrum is in need of unfolding.

[3] In particle physics analyses, "truth" or "truth information" is in general an expression used for the generated event information coming from the Monte Carlo simulation at "particle level", i.e., before the detector response is accounted for [56, 57].

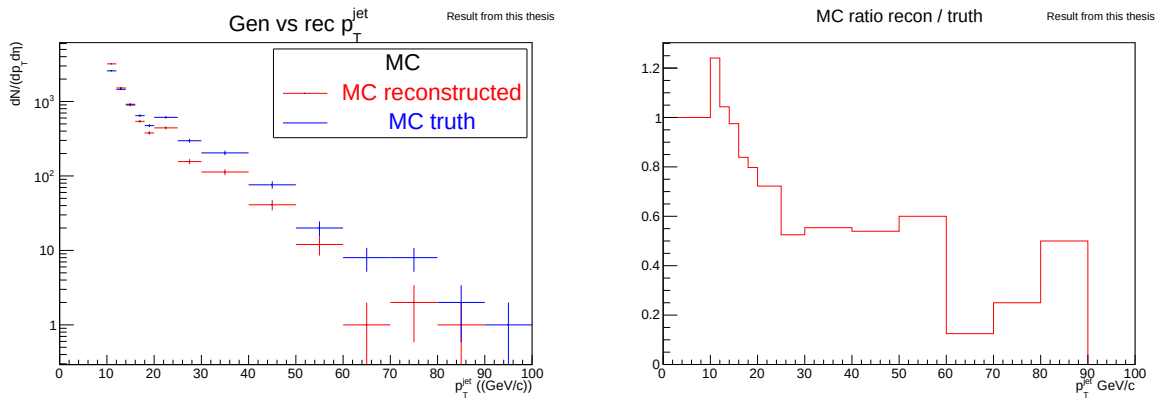

Figure 4.9: Comparison (left) of the generator level MC truth spectrum (blue) and the detector level MC reconstructed spectrum (red). Ratio (right) of MC reconstructed spectrum over the MC truth spectrum. In principle, given a "perfect" detector response, this ratio should be one. The spectra are plotted with a logarithmic scale for the yields.

After the unfolding process, the resulting spectra represent a closer approximation to the actual event. The result of the unfolding procedure, together with the raw measured jet spectrum, can be seen in Figure 4.10 on the left. As expected, the unfolded spectrum is similar, yet larger than the measured spectrum. The unfolding shifts the measured spectrum to slightly higher values, as is expected due to the loss of jets which were not detected. On the right, the ratio between the measured spectra before and after unfolding is shown.

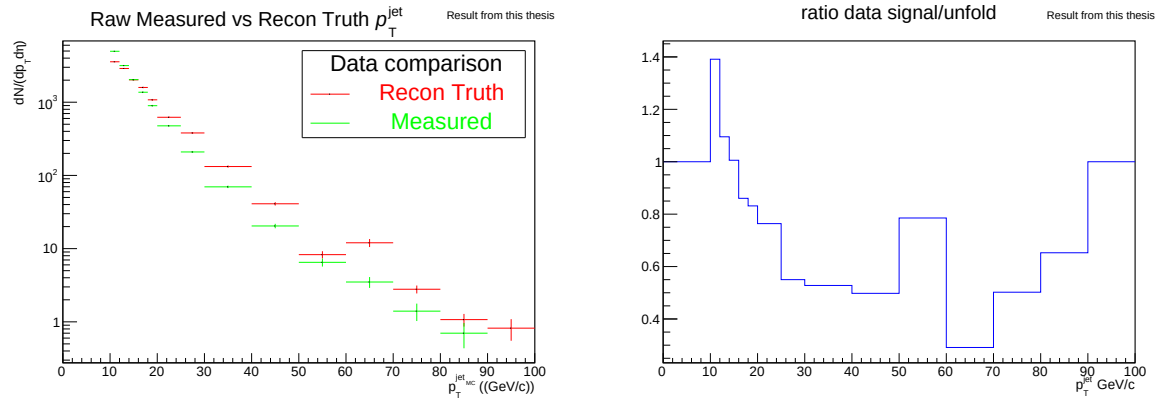

Figure 4.10: Plot (left) of the unfolded p_T spectrum (red) together with the measured spectrum (green). The spectra are plotted with a logarithmic scale for the yields. Ratio (right) of the unfolded p_T spectrum to the raw measured spectrum.

4.7.1 Response matrix

The detector response matrix is constructed from full MC simulations. To construct the response matrix, particle level jets and detector level jets are reconstructed and matched.

The matrix is found using AliReducedVarManager::kJetPt as well as AliReducedVarManager::kJetPtMC, with the same cut parameters as the jetCutDefault.
The jet matching requires a maximum matching distance of 0.3, taking only the spatial distance between the jets into account. In addition, a 1-1 correspondence is required. The response matrix is a 2D histogram containing the p_{T} distributions of reconstructed particle level jets and generator level jets. Figure 4.11 shows the response matrix with binning matching the bins of the raw p_{T} spectra in data. As can be observed, the response matrix suffers from low statistics, especially at high p_{T}.

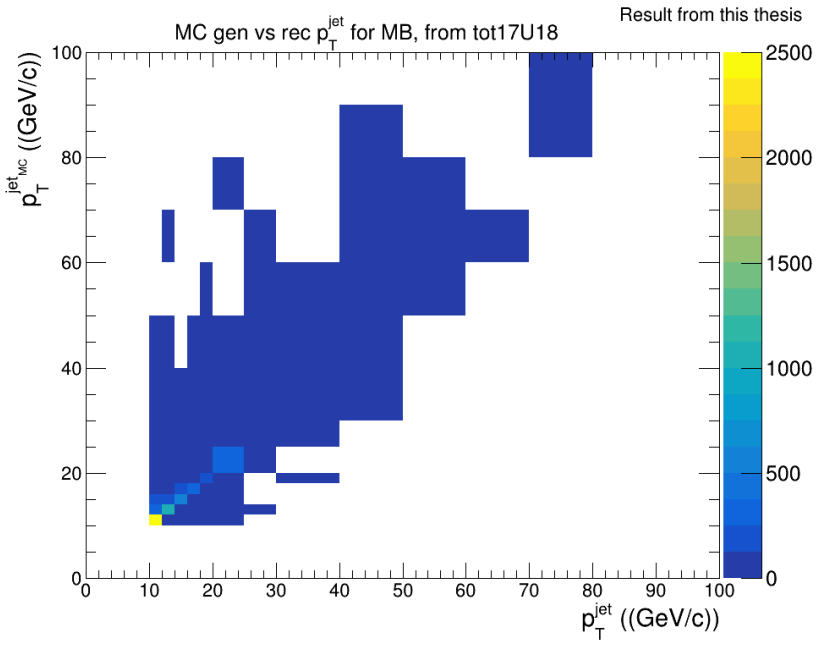

Figure 4.11: Response matrix for the MC simulation showing particle level generated jets along the y-axis and the detector level reconstructed jets along the x-axis.

4.7.2 MC Closure test

To determine the stability of the unfolding, a closure test is performed on the unfolding procedure [58]. In this step, the MC data set is separated into two statistically independent samples, that is, MC simulations for 2017 and MC simulations for 2018, respectively. The reconstructed jet spectrum in the 2017 MC sample, is given as input spectrum and the response matrix is constructed using the MC 2018 sample. The unfolded result is then compared to the generated level jets in the 2017 MC sample. If the unfolding is successful, it should have corrected the reconstructed level jets of the 2017 MC sample to its generated level values. The results of the MC closure test is shown in Figure 4.12.

The reconstructed level 2017 MC spectrum (green lines), is as expected lower than that of the generated level 2017 MC spectrum (blue lines). The spectra after unfolding is represented by the red lines. Thus, we see that the unfolding process shifts the recorded spectra to much closer approximate the truth spectrum. The unfolding procedure shows greater accuracy for low p_{T} bins than for the higher p_{T} bins. For high p_{T}, the unfolding shifts the values in the right direction, but we still observe some differences between reconstructed unfolded spectrum and generated spectrum.

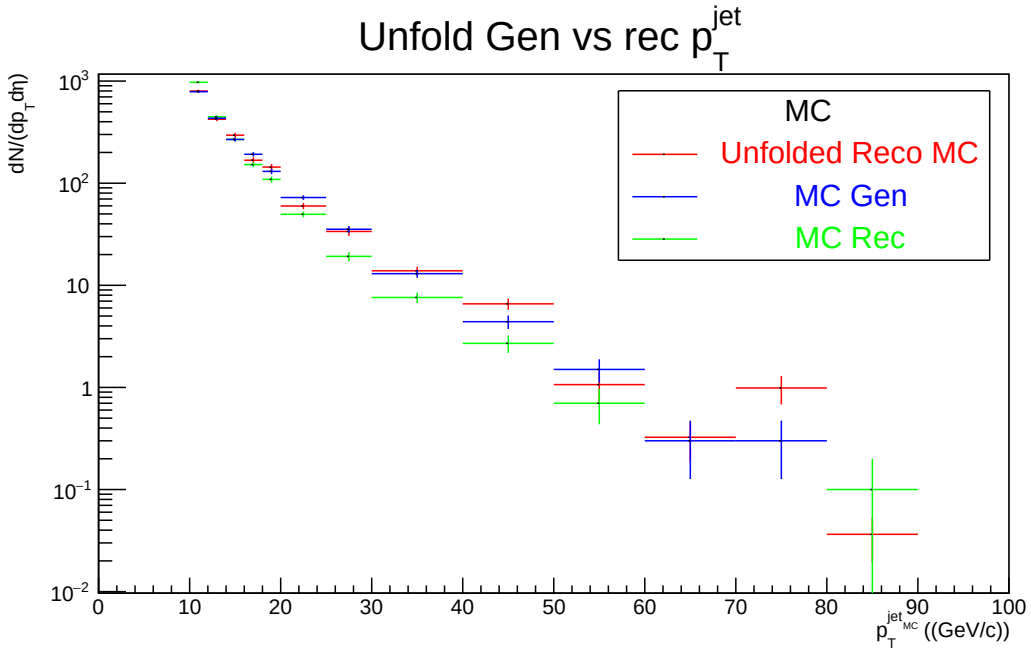

Figure 4.12: Result of closure procedure for unfolding. The blue lines indicate the LHC17 MC particle level generated events, the green indicate LHC17 MC detector level reconstructed events, and red indicates the unfolded reconstructed events. The spectra are plotted with a logarithmic scale for the simulated truth and yields.

In Figure 4.13, the ratio between reconstructed spectrum after unfolding to generated spectrum is shown. Given an ideal unfolding, the ratio should be close to unity. For the lower p_{T} bins, this seems to be the case. However, for the higher bins, especially the 60-70 p_{T} range, there are greater deviations, which likely stems from a lack of sufficient statistics in the data sample. However, mostly the unfolding is within 20% of unity.

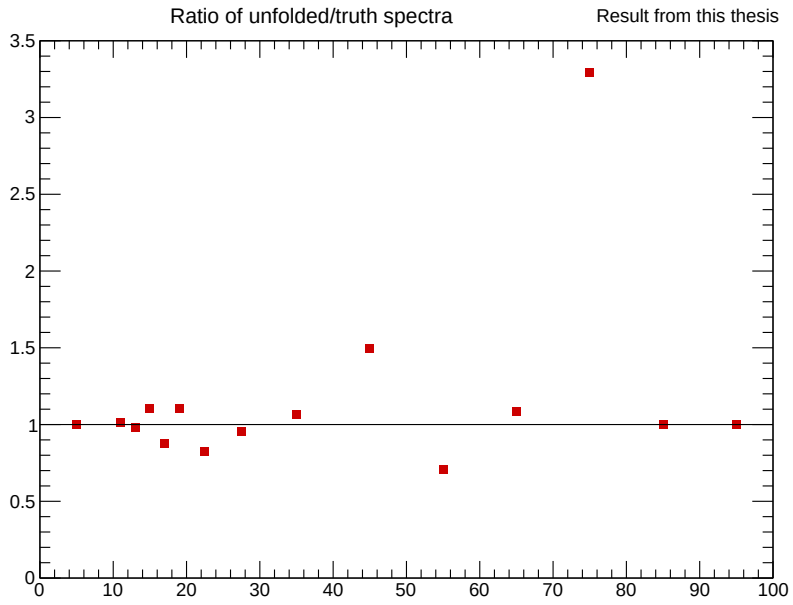

Figure 4.13: Stability check of the unfolding procedure, comparing the unfolded MC spectrum to the MC truth spectrum. For a perfect unfolding, this would align to 1.

4.7.3 Luminosity

Reference Cross Section

Luminosity in ALICE is determined from detection of cross sections through a method known as a van der Meer scan (vdM) [59]. The measured cross section, or 'visual' cross section σ_{vis}, is not expected to be the actual cross section of the experiment system, but rather a fraction of the actual inelastic interaction cross section. The formula is as follows [60]:

$$\sigma_{\text{vis}} = \epsilon \sigma_{\text{inel}},$$

where ϵ is the fraction of inelastic events that satisfy the trigger condition, and the total inelastic interaction cross section is denoted σ_{inel}.

The luminosity is then determined as follows:

$$\mathcal{L} = \frac{N_1 N_2 f_{rev}}{h_x h_y},$$

where N_1 and N_2 are the particle intensities, determined from measurements of a given process rate R as a function of the beam separation Δx and Δy, and f_{rev} is the accelerator revolution frequency. The reference cross section σ_R is given by:

$$\sigma_R = \frac{R(0,0)}{\mathcal{L}} ,$$

where $R(0,0)$ is the head-on rate.

For this analysis, a reference cross section σ_{V0AND} is used. For the $\sqrt{s} = 13$ TeV 2017 and 2018 runs, the reference cross section for pp collisions is [60]:

$$\sigma_{\mathrm{V0AND}}^{\mathrm{LHC17}} = 58.10 \pm 2.7 \text{ mb}, \;\; \sigma_{\mathrm{V0AND}}^{\mathrm{LHC18}} = 57.52 \pm 2.1 \text{ mb}.$$

Integrated Luminosity

The integrated luminosity, needed in this analysis as a sample specific correction of the recorded luminosity, is found through, with i representing each run number,

$$\mathcal{L}_{\mathrm{Int}}^{\mathrm{MB},\,i} = \frac{N_{MB}^{\mathrm{corr},\,i}}{\sigma_{\mathrm{V0AND}}} , \tag{4.1}$$

where σ_{V0AND} is taken from an official determination of cross section [60], and N_{MB}^{corr} is the number of Minimum Bias events including events with and without a reconstructed vertex within the vertex requirement of $|z| < 10$ cm. This number can only be estimated, as the analyzed events require a reconstructed vertex. Based on the assumption that events without a reconstructed vertex follow the same vertex distribution as events with a reconstructed vertex, the total number of events is estimated by taking the fraction f_z^i of selected events with a reconstructed vertex within the z-vertex requirement over the selected events without a z-veretx requirement. Thus, the number of events with and without a reconstructed vertex is given by,

$$N_{\mathrm{MB}}^{\mathrm{corr},\,i} = \sum_i f_z^i \cdot N_{\mathrm{MB}}^{\mathrm{sel},\,i} , \tag{4.2}$$

where $\sum f_z^i$ is a correction of the luminosity and $N_{\mathrm{MB}}^{\mathrm{sel},\,i}$ is the number of selected events with a reconstructed vertex. Stated more intuitively,

$$\sum f_z^i = \frac{N_{\mathrm{MB}}^{\mathrm{sel},\,i}(|z_{\mathrm{vtx}}| < 10\ \mathrm{cm})}{N_{\mathrm{MB}}^{\mathrm{corr},\,i}(|z_{\mathrm{vtx}}| < \infty)}\,. \tag{4.3}$$

The correction factor f_z^i is determined from a Gaussian fit to the z-vertex distribution in each run. Figure 4.14 shows the z-vertex distribution for run 273103 with a Gaussian fit on the left, and the total result of the Gaussian fit calculation of f_z for each run in the data sample on the right.

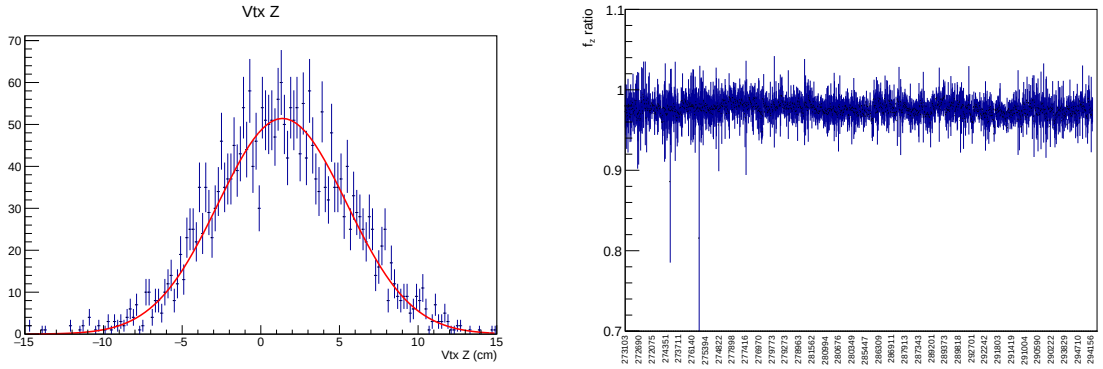

Figure 4.14: The z-vertex distribution (left) for the LHC17h run 273103. The red curve represents the Gaussian fit for this run. The calculated f_z (right) for all runs in the MB data sample.

The integrated luminosity of the TRD triggered data is determined in a similar manner as for the MB data, but with an additional trigger normalization f_{norm}. The integrated luminosity is determined as

$$\mathcal{L}_{\mathrm{Int}}^{\mathrm{TRD},\,i} = \frac{N_{\mathrm{TRD}}^{\mathrm{corr},\,i} \cdot f_{\mathrm{norm}}^i}{\sigma_{\mathrm{V0AND}}}\,, \tag{4.4}$$

where $N_{\mathrm{TRD}}^{\mathrm{corr},\,i}$ is similarly defined for TRD as (4.2) is for MB and f_{norm}^i is a further correction from the number of MB events such that

$$\frac{1}{f_{\mathrm{norm}}^i} = \frac{N_{\mathrm{MBandTRD}}^i}{N_{\mathrm{MB}}^i}\,, \tag{4.5}$$

where N_{MBandTRD}^i is the number of events (per run i) in the MB sample which also satisfy the TRD requirements. As N_{MBandTRD}^i is a subsample of N_{MB}^i one can by taking the inverse of the trigger normalization use a Binomial error calculation.

The total integrated luminosity for the complete LHC17 and LHC18, MB triggered data sample is:

$$\mathcal{L}_{\mathrm{Int}}^{\mathrm{MB}} = 0.224 \pm 1.8\% \,(\mathrm{syst})\,\mathrm{nb}^{-1}\,, \tag{4.6}$$

and for the TRD triggered data sample is:

$$\mathcal{L}_{\mathrm{Int}}^{\mathrm{TRD}} = 0.183 \pm 1.8\% \,(\mathrm{syst})\,\mathrm{nb}^{-1}\,, \tag{4.7}$$

where the statistical errors are found to be negligible in both cases.

Chapter 5

Results and outlook

5.1 Results

In this chapter, the charged jet cross section at $\sqrt{s} = 13$ TeV will be presented. Both the MB and TRD triggered jet p_{T} spectra will be discussed and compared. Lastly, the MB cross section result will be compared to a published ALICE result [14] at the same energy.

5.1.1 Charged Jet Cross Section

The plots in Section 4 are the result of this thesis's analysis, taken from a specially selected set of data taking runs, applied with a specific set of cuts. For the analysis result to be meaningfully comparable with other results of similar nature, a *cross section normalisation* must be applied. The p_{T}-differential charged jet cross section is determined by:

$$\frac{d^2\sigma^{\text{jet, ch}}}{dp_{\mathrm{T}}d\eta} = \frac{\Delta N_{\text{meas}}^{\text{jet, ch}}}{\Delta\eta\Delta p_{\mathrm{T}}} \cdot \frac{1}{\mathcal{L}_{\text{int}}}, \tag{5.1}$$

where $\Delta N_{\text{meas}}^{\text{jet, ch}}$ is the measured jet spectra after unfolding and $\mathcal{L}_{\text{int}}$ is the integrated luminosity given by Equation (4.1) for MB data and (4.4) for TRD data. Figure 5.1 shows

the normalised cross section, found using the unfolded MB jet spectra in Section 4.7, and applying the integrated luminosity found as described in Section 4.7.3 for scaling. The TRD cross section is found similarly and is shown in Figure 5.2.

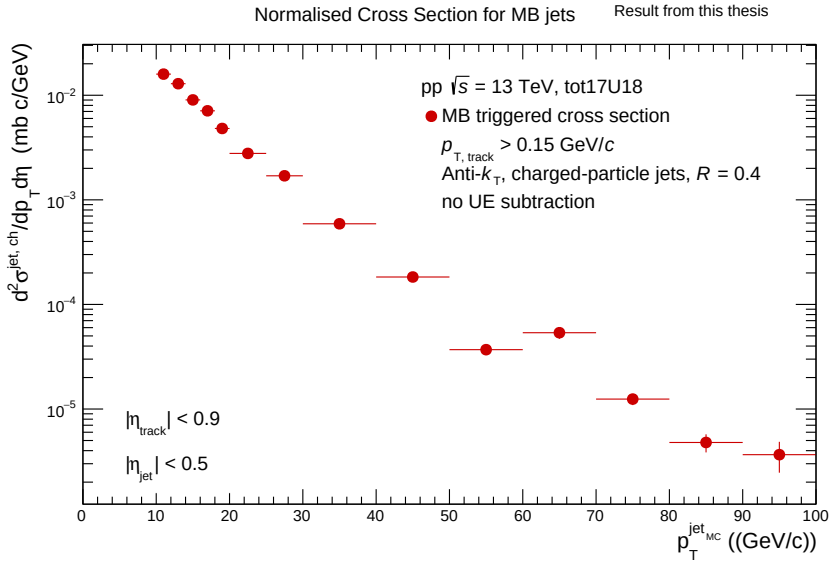

Figure 5.1: Normalised cross section for MB triggered jets in LHC17 and LHC18, found from the unfolded MB jet spectra in section 4.7, using the integrated luminosity found as described in section 4.7.3 for scaling.

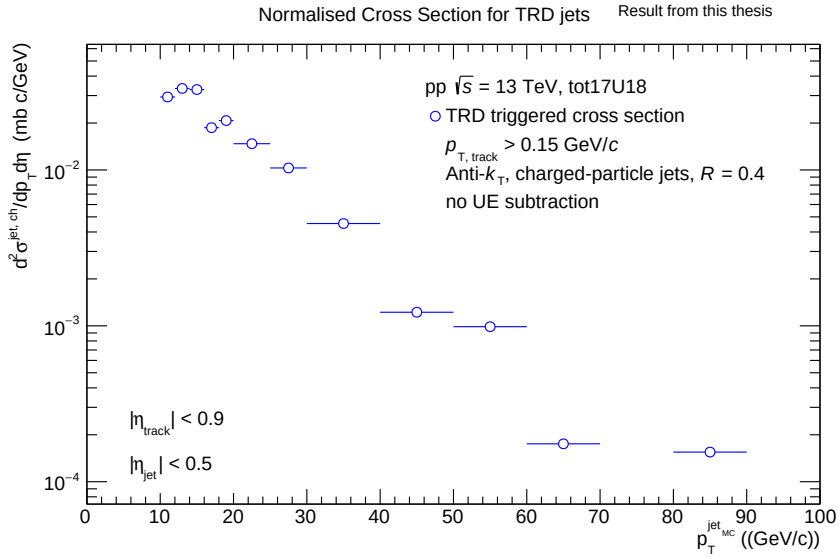

Figure 5.2: Normalised cross section for TRD triggered jets in LHC17 and LHC18, found from the unfolded TRD jet spectra in section 4.7, using the integrated luminosity found as described in section 4.7.3 for scaling.

The normalised cross section for both MB and TRD is plotted together in Figure

5.3. After both unfolding and integrated luminosity corrections, we observe a larger cross section for the TRD trigger than the MB trigger. Due to the limited statistics in the unfolding response matrix, the TRD triggered spectrum shows some fluctuations.

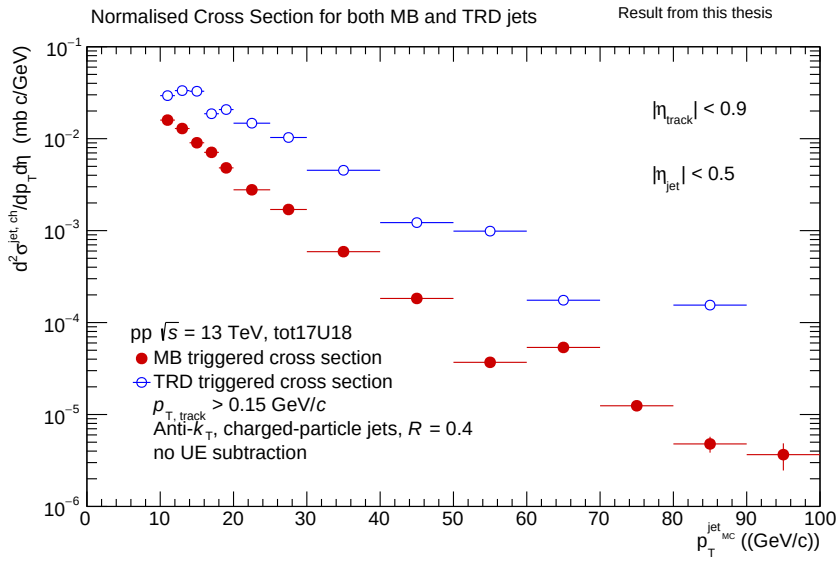

Figure 5.3: Normalised cross section for both MB (red) and TRD (blue) in the total LHC17 and LHC18 data sample, found from the unfolded MB and TRD jet spectra in section 4.7, using the integrated luminosities found as described in section 4.7.3 for scaling.

A similar comparison to the one made between the raw jet spectra of MB and TRD has been made for the jet cross sections. The difference in jet cross section between TRD and MB triggers can be seen in Figure 5.4. Here, for each bin, the MB cross section value is simply subtracted from the TRD cross section value. This is a more physically meaningful comparison than the one made in Section 4.6, as it takes into account the different size of the two data samples. The ratio of the TRD cross section to the MB cross section can be seen in Figure 5.5. The growing ratio means that there is a hardening of the TRD cross section with respect to the MB cross section. The significant jump in the 60-70 p_{T} bin could come from a lack of sufficient statistics as well, as we saw in the unfolding.

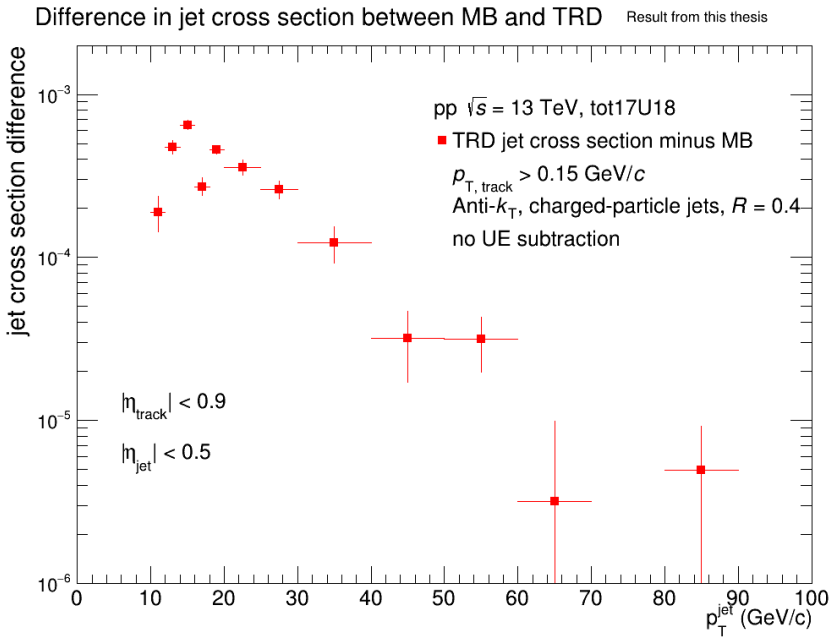

Figure 5.4: Difference in the normalised cross sections of TRD and MB jets shown in Figure 5.3.

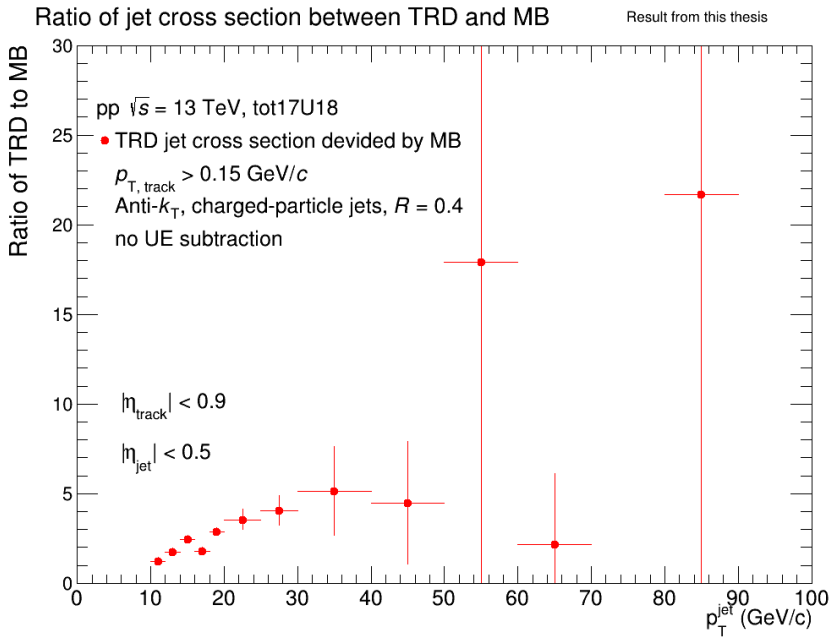

Figure 5.5: Ratio of the normalised cross sections of TRD triggered and MB triggered jets.

5.1.2 ALICE Published Cross Section Comparison

In figure 5.6 the MB triggered charged jet cross section is compared to the published ALICE measurement of charged jets at $\sqrt{s} = 13$ TeV [14]. For the ALICE measured spectrum in blue, statistical uncertainties are shown as error bars, and the systematic uncertainties are shown as boxes. For the result of this thesis shown in red, only statistical uncertainties are shown. The MB triggered result of this thesis is produced using the framework built for the J/ψ finding, thus comparing the result with the published measurement at the same energy serves to validate the robustness of the new framework. As seen, for $p_{\mathrm{T}} > 20$ GeV/c the results are compatible, while some deviations are seen at lower p_{T}. The choice of minimum track p_{T}, track rapidity $|\eta_{\mathrm{track}}| < 0.9$, as well as cone radius $R = 0.4$, is the same in the published result as for this thesis. One should note, however, that the published cross section is made with subtraction of UE as well, while the thesis cross section is made with no UE subtraction. Furthermore, the published cross section is produced from significantly more statistics and with a much more stable unfolding procedure. The difference in cross section at lower p_{T} might be attributable to the requirement of a leading track with p_{T} above 5 GeV/c, which is applied for the result of this thesis, and not applied for the ALICE published result. For jets at lower p_{T}, this leading track requirement rejects more jets than for higher p_{T} jets, as high p_{T}-jets are more likely to have leading tracks with high p_{T}. At higher p_{T}, the greatest deviation from the published result is in the 60-70 p_{T} bin, which as discussed is likely stemming from insufficient statistics in the unfolding process.

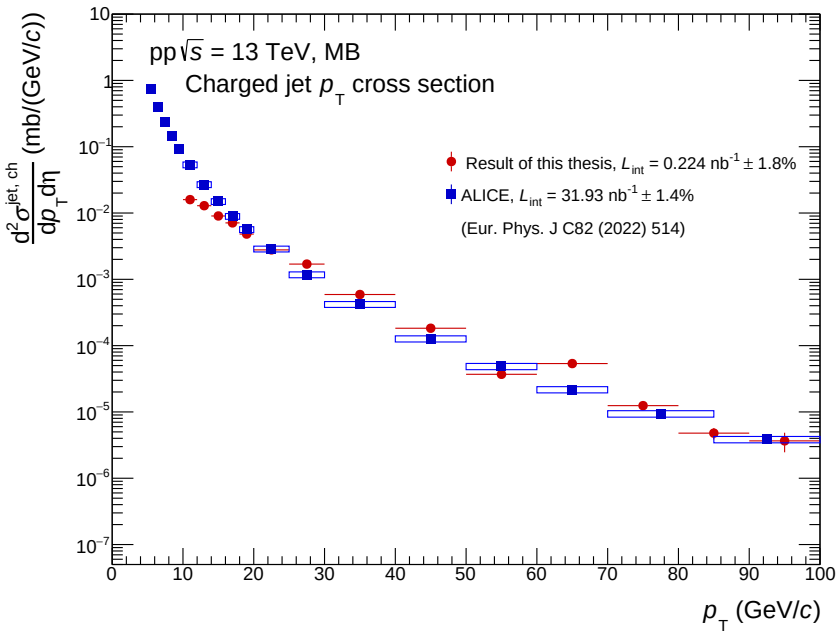

Figure 5.6: Comparison between an ALICE published cross section (blue) [14] and the cross section found in this thesis (red).

5.2 Outlook

This thesis presents the charged jet cross section with statistical uncertainties. However, no calculation of systematic uncertainties was considered in this measurement. Future studies should include the determination of systematic uncertainties, such as uncertainties due to tracking efficiency and resolution and the unfolding procedure. Uncertainties on the tracking efficiency and resolution could be done by propagating the single track efficiency to the measured jet spectrum using an MC simulation and varying the detector efficiency and resolution. In addition, the systematic uncertainty due to the hybrid track selection can be estimated by varying the tracking cuts used in the analysis.

For further studies, a standard jet analysis would benefit from using a jet-injected MC sample. As previously mentioned, the unfolding relies on a detector response matrix with limited statistics. With jet-injections in the MC sample, this would give better statistics for the detector response described in Section 4.7.1 and likely lead to a more valid unfolding. As mentioned in Section 4.7, the analysis in this thesis used the Bayesian method of unfolding, with four iterations. A possible way to improve the performance of the unfolding procedure would be to run the full set of iterations multiple times in what has been referred to as "super-iterations" [61].

There are several different available unfolding methods in the RooUnfold package. Examples include the Singular Value Decomposition (SVD), as used in the ALICE publication [14], and the TUnfold method, using the unfolding class TUnfold implemented in the ROOT software, a bin-by-bin method, and an inverted response matrix method. For a more thorough analysis, a selection of these methods should be applied separately, and each method tested with the MC closure test.

The analysis in this thesis has been an important test of the framework implemented for further studies of J/ψ in jets. The framework seems stable, giving a jet spectrum which is compatible with what we would expect, as seen with the published ALICE [14] comparison in Section 5.1.2. As mentioned, the cross section in this thesis was determined with no UE subtraction. Even though the effect of UE activity in pp collisions on jet measurement is rather limited, a full analysis would benefit from UE event subtraction, as the UE contribution affects different events according to their multiplicity [14]. We also observed some differences in the spectra at low p_{T} which are likely due to the requirement on the $p_{\mathrm{T}} > 5$ GeV/c of the leading jet track. This requirement is applied to limit the possibilities of fake (very soft) jets, which in the case of UE subtraction is less important.

As jets are highly variable structures, variations on the radius R of the jet definition would serve to uncover biases resulting from the chosen jet reconstruction parameters. Typical values for R are single digit variations from 0.2 to 0.7.

In conclusion, the analysis in this thesis shows that the jet framework seems to be working as expected, but more work needs to be done when considering the unfolding process. The unfolding procedure requires sufficient statistics, and the closure test should give values closer to one. Various unfolding methods should be tested, and the composition of the response matrix should be taken into account.

Bibliography

[1] M. Thomson, "Modern particle physics", Cambridge University Press, 2013.

[2] B.-J. Schaefer and M. Wagner, "On the QCD phase structure from effective models", *Prog. Part. Nucl. Phys.* **62** (2009) 381, arXiv:0812.2855.

[3] Z. L. Matthews, "Flow". 2022-09-15. http://www.quantumdiaries.org/2011/11/07/flow/

[4] **ALICE**, K. Aamodt *et al.*, "Higher harmonic anisotropic flow measurements of charged particles in Pb-Pb collisions at $\sqrt{s_{NN}}$=2.76 TeV", *Phys. Rev. Lett.* **107** (2011) 032301, arXiv:1105.3865.

[5] **ALICE**, J. Adam *et al.*, "Anisotropic flow of charged particles in Pb-Pb collisions at $\sqrt{s_{\rm NN}} = 5.02$ TeV", *Phys. Rev. Lett.* **116** (2016), no. 13, 132302, arXiv:1602.01119.

[6] G. P. Salam, "Elements of QCD for hadron colliders", in "2009 European School of High-Energy Physics". 11 2010. arXiv:1011.5131.

[7] K. Tywoniuk, "Relativistic heavy-ion physics, PHYS333. III Hard probes, jets and jet quenching". 2022.09.16. https://mitt.uib.no/courses/35472/files/folder/Lecture%20Notes?preview=4230279

[8] **CMS**, S. Chatrchyan *et al.*, "Observation and studies of jet quenching in PbPb collisions at nucleon-nucleon center-of-mass energy = 2.76 TeV", *Phys. Rev. C* **84** (2011) 024906, arXiv:1102.1957.

[9] V. Frigo, "LHC map in 3D. Schéma du LHC en 3D", AC Collection. Legacy of AC. Pictures from 1992 to 2002., 1997, unpublished. http://cds.cern.ch/record/842700

[10] **ALICE**, K. Aamodt *et al.*, "The ALICE experiment at the CERN LHC", *JINST* **3** (2008) S08002.

[11] **ALICE**, B. B. Abelev *et al.*, "Performance of the ALICE Experiment at the CERN LHC", *Int. J. Mod. Phys. A* **29** (2014) 1430044, arXiv:1402.4476.

[12] **ALICE**, P. Cortese *et al.*, "ALICE: Physics performance report, volume I", *J. Phys. G* **30** (2004) 1517–1763.

[13] A. Andronic, "ALICE TRD - Picture Gallery". 2022.09.27. http://www-alice.gsi.de/trd/gallery/index.html

[14] **ALICE**, S. Acharya *et al.*, "Multiplicity dependence of charged-particle jet production in pp collisions at $\sqrt{\mathbf{s}} = \mathbf{13}$ **TeV**", *Eur. Phys. J. C* **82** (2022), no. 6, 514, arXiv:2202.01548.

[15] T. Muta, "Foundations of Quantum Chromodynamics: An Introduction to Perturbative Methods in Gauge Theories, (3rd ed.)", World Scientific, Hackensack, N.J., 3rd ed., 2010.

[16] Y. P. Goncharov, *Quark confinement mechanism for baryons*, pp. 13–61. 2013. arXiv:1312.4049.

[17] E. Eichten, K. Gottfried, T. Kinoshita, J. Kogut, K. D. Lane, and T. M. Yan, "Spectrum of Charmed Quark-Antiquark Bound States", *Phys. Rev. Lett.* **34** Feb (1975) 369–372.

[18] R. Rapp and H. van Hees, "Heavy Quark Diffusion as a Probe of the Quark-Gluon Plasma", arXiv:0803.0901.

[19] S. Schuchmann, "Modification of K^0_s and $\Lambda(\bar{\Lambda})$ transverse momentum spectra in Pb-Pb collisions at $\sqrt{s_{NN}} = 2.76$ TeV with ALICE", PhD thesis, Goethe U., Frankfurt (main), 2015.

[20] A. Deur, S. J. Brodsky, and G. F. de Teramond, "The QCD Running Coupling", *Nucl. Phys.* **90** (2016) 1, arXiv:1604.08082.

[21] D. J. Gross and F. Wilczek, "Ultraviolet Behavior of Nonabelian Gauge Theories", *Phys. Rev. Lett.* **30** (1973) 1343–1346.

[22] H. D. Politzer, "Reliable Perturbative Results for Strong Interactions?", *Phys. Rev. Lett.* **30** (1973) 1346–1349.

[23] **Particle Data Group**, K. A. Olive *et al.*, "Review of Particle Physics", *Chin. Phys. C* **38** (2014) 090001.

[24] U. W. Heinz and M. Jacob, "Evidence for a new state of matter: An Assessment of the results from the CERN lead beam program", `nucl-th/0002042`.

[25] P. Braun-Munzinger and J. Stachel, "The quest for the quark-gluon plasma", *Nature* **448** (2007) 302–309.

[26] **PHOBOS**, B. B. Back *et al.*, "The PHOBOS perspective on discoveries at RHIC", *Nucl. Phys. A* **757** (2005) 28–101, `nucl-ex/0410022`.

[27] "CERN Completes Transition to Lead-Ion Running at the LHC (Press release)", 2010. 2022-08-30. `https://press.cern/news/press-release/cern/cern-completes-transition-lead-ion-running-lhc`

[28] "New State of Matter created at CERN", 2000. 2022-09-12. `https://home.web.cern.ch/news/press-release/cern/new-state-matter-created-cern`

[29] U. W. Heinz, "The Little bang: Searching for quark gluon matter in relativistic heavy ion collisions", *Nucl. Phys. A* **685** (2001) 414–431, `hep-ph/0009170`.

[30] **ALICE**, J. Adam *et al.*, "Transverse momentum dependence of D-meson production in Pb-Pb collisions at $\sqrt{s_{NN}} = 2.76$ TeV", *JHEP* **03** (2016) 081, `arXiv:1509.06888`.

[31] F.-M. Liu and S.-X. Liu, "Quark-gluon plasma formation time and direct photons from heavy ion collisions", *Phys. Rev. C* **89** (2014), no. 3, 034906, `arXiv:1212.6587`.

[32] M. L. Miller, K. Reygers, S. J. Sanders, and P. Steinberg, "Glauber modeling in high energy nuclear collisions", *Ann. Rev. Nucl. Part. Sci.* **57** (2007) 205–243, `nucl-ex/0701025`.

[33] T. Niida and Y. Miake, "Signatures of QGP at RHIC and the LHC", *AAPPS Bull.* **31** (2021), no. 1, 12, `arXiv:2104.11406`.

[34] M. Cacciari, G. P. Salam, and G. Soyez, "FastJet User Manual", *Eur. Phys. J. C* **72** (2012) 1896, `arXiv:1111.6097`.

[35] G. P. Salam and G. Soyez, "A Practical Seedless Infrared-Safe Cone jet algorithm", *JHEP* **05** (2007) 086, arXiv:0704.0292.

[36] M. Cacciari, G. P. Salam, and G. Soyez, "The anti-k_t jet clustering algorithm", *JHEP* **04** (2008) 063, arXiv:0802.1189.

[37] L. Gyulai, S. Sándor, and R. Vértesi, "Defining the Underlying-Event Activity in the Presence of Heavy-Flavour Processes in Proton-Proton Collisions at LHC Energies", *Particles* **5** (2022), no. 3, 235–244, arXiv:2206.00367.

[38] M. Cacciari, G. P. Salam, and G. Soyez, "The Catchment Area of Jets", *JHEP* **04** (2008) 005, arXiv:0802.1188.

[39] J. D. Bjorken, "Energy Loss of Energetic Partons in Quark - Gluon Plasma: Possible Extinction of High p(t) Jets in Hadron - Hadron Collisions", 8 1982.

[40] M. Benedikt, P. Collier, V. Mertens, J. Poole, and K. Schindl, "LHC Design Report", CERN, Geneva, 2004.

[41] **ALICE**, N. Antoniou *et al.*, "Letter of Intent for A Large Ion Collider Experiment", 3 1993.

[42] "The history of CERN, The Large Hadron Collider". 2022-09-18. https://timeline.web.cern.ch/taxonomy/term/89?page=2

[43] "Performance of the ALICE experiment at the CERN LHC", *International Journal of Modern Physics A* **29** sep (2014) 1430044.

[44] **ALICE**, E. Abbas *et al.*, "Performance of the ALICE VZERO system", *JINST* **8** (2013) P10016, arXiv:1306.3130.

[45] **DPG - Data Preparation Group**, "Alice data flow". 2022-09-17. https://indico.cern.ch/event/666222/contributions/2768780/attachments/1551303/2437229/DPG_AnalysisTutorial_20171102.pdf

[46] **ALICE**, "AliRoot package". https://github.com/alisw/AliRoot, . 2022-09-16.

[47] **ALICE**, "ALICE analysis repository". https://github.com/alisw/AliPhysics/, . 2022-09-16.

[48] "ROOT: analyzing petabytes of data, scientifically.". https://root.cern.ch/. 2022-09-16.

[49] T. Sjostrand, S. Mrenna, and P. Z. Skands, "A Brief Introduction to PYTHIA 8.1", *Comput. Phys. Commun.* **178** (2008) 852–867, arXiv:0710.3820.

[50] **GEANT4**, S. Agostinelli *et al.*, "GEANT4–a simulation toolkit", *Nucl. Instrum. Meth. A* **506** (2003) 250–303.

[51] "MonALISA - the ALICE Grid monitoring toolset". 2022-09-17. https://alice-doc.github.io/alice-analysis-tutorial/analysis/monalisa.html

[52] M. Cacciari and G. P. Salam, "Pileup subtraction using jet areas", *Phys. Lett. B* **659** (2008) 119–126, arXiv:0707.1378.

[53] "Informations on track selection for AOD147". https://twiki.cern.ch/twiki/bin/viewauth/ALICE/AddTaskInfoAOD147. 2022-09-17.

[54] **ALICE**, S. Acharya *et al.*, "Production of deuterons, tritons, ^{3}He nuclei and their antinuclei in pp collisions at $\sqrt{s} = 0.9$, 2.76 and 7 TeV", *Phys. Rev. C* **97** (2018), no. 2, 024615, arXiv:1709.08522.

[55] "RooUnfold". https://gitlab.cern.ch/RooUnfold/RooUnfold. 2022-09-25.

[56] A. Buckley *et al.*, "General-purpose event generators for LHC physics", *Phys. Rept.* **504** (2011) 145–233, arXiv:1101.2599.

[57] J. M. Butterworth *et al.*, "THE TOOLS AND MONTE CARLO WORKING GROUP Summary Report from the Les Houches 2009 Workshop on TeV Colliders", in "6th Les Houches Workshop on Physics at TeV Colliders". 3 2010. arXiv:1003.1643.

[58] Y. Wu, "Measurement of the production of $\mathrm{D_s^+}$ mesons in charged jets in proton-proton collisions at $\sqrt{s} = 13$ TeV". https://alice-notes.web.cern.ch/node/1325. 2022.09.28.

[59] S. van der Meer, "Calibration of the Effective Beam Height in the ISR", 6 1968.

[60] **ALICE Collaboration**, "ALICE 2016-2017-2018 luminosity determination for pp collisions at $\sqrt{s} = 13$ TeV", 2021.

[61] **CMS**, A. Tumasyan *et al.*, "Fragmentation of jets containing a prompt J/ψ meson in PbPb and pp collisions at $\sqrt{s_{\mathrm{NN}}} = 5.02$ TeV", *Phys. Lett. B* **825** (2022) 136842, arXiv:2106.13235.

Appendix A

Runlists used for analysis

LHC18b: RunList_LHC18b_pass2_MB (27 runs)
285447, 285396, 285365, 285364, 285347, 285328, 285327, 285224, 285222, 285203, 285202, 285200, 285165, 285127, 285108, 285106, 285066, 285065, 285064, 285015, 285014, 285013, 285012, 285011, 285010, 285009, 285008

LHC18d: RunList_LHC18d_pass2_MB (46 runs)
286350, 286349, 286348, 286345, 286341, 286340, 286337, 286336, 286314, 286313, 286312, 286311, 286310, 286309, 286308, 286289, 286288, 286287, 286284, 286282, 286263, 286261, 286258, 286257, 286231, 286230, 286229, 286203, 286202, 286201, 286199, 286198, 286159, 286130, 286129, 286127, 286124, 286064, 286030, 286028, 286027, 286025, 286014, 285980, 285979, 285978,

LHC18e: RunList_LHC18e_pass2_MB (41 runs)
286937, 286936, 286933, 286932, 286931, 286930, 286911, 286910, 286877, 286876, 286874, 286852, 286850, 286846, 286809, 286805, 286801, 286799, 286731, 286695, 286661, 286653, 286633, 286592, 286591, 286569, 286568, 286567, 286566, 286511, 286509, 286508, 286502, 286501, 286482, 286455, 286454, 286428, 286427, 286426, 286380,

LHC18f: RunList_LHC18f_pass2_MB (72 runs)
287977, 287975, 287941, 287923, 287915, 287913, 287912, 287911, 287885, 287884, 287883, 287877, 287876, 287784, 287658, 287657, 287656, 287654, 287578, 287575, 287524, 287518, 287517, 287516, 287513, 287486, 287484, 287481, 287480, 287451, 287413, 287389, 287388, 287387, 287385, 287381, 287380, 287360, 287356, 287355, 287353, 287349, 287347, 287346, 287344, 287343, 287325, 287324, 287323, 287283, 287254, 287251, 287250, 287249, 287248, 287209, 287208, 287204, 287203, 287202, 287201, 287185, 287155, 287137, 287077, 287072, 287071, 287066, 287064, 287063, 287021, 287000,

LHC18g: RunList_LHC18g_pass2_MB (11 runs)
288750, 288748, 288743, 288690, 288689, 288687, 288650, 288644, 288642, 288640, 288619,

LHC18h: RunList_LHC18h_pass2_MB (2 runs)
288804, 288806,

LHC18k: RunList_LHC18k_pass2_MB (12 runs)
289201, 289200, 289199, 289198, 289177, 289176, 289175, 289172, 289169, 289167, 289166, 289165,

LHC18l: RunList_LHC18l_pass2_MB (88 runs)
289240, 289241, 289242, 289247, 289249, 289253, 289254, 289275, 289276, 289277, 289278, 289280, 289281, 289300, 289303, 289306, 289308, 289309, 289353, 289354, 289355, 289356, 289365, 289366, 289367, 289368, 289369, 289370, 289373, 289374, 289426, 289444, 289462, 289463, 289465, 289466, 289468, 289493, 289494, 289521, 289547, 289574, 289576, 289577, 289582, 289625, 289632, 289634, 289657, 289658, 289659, 289660, 289664, 289666, 289721, 289723, 289724, 289729, 289731, 289732, 289757, 289775, 289808, 289811, 289814, 289815, 289816, 289817, 289818, 289830, 289849, 289852, 289854, 289855, 289856, 289857, 289879, 289880, 289884, 289928, 289931, 289935, 289940, 289941, 289943, 289965, 289966, 289971,

LHC18m: RunList_LHC18m_pass2_MB (261 runs)
292839, 292836, 292834, 292832, 292831, 292811, 292810, 292809, 292804, 292803, 292758, 292754, 292752, 292750, 292748, 292747, 292744, 292739, 292737, 292704, 292701, 292698, 292696, 292695, 292693, 292586, 292584, 292563, 292560, 292559, 292557, 292554, 292553, 292526, 292524, 292523, 292521, 292500, 292497, 292496, 292495, 292461, 292460, 292457, 292456, 292434, 292432, 292430, 292429, 292428, 292406, 292405, 292398, 292397, 292298, 292274, 292273, 292270, 292269, 292265, 292242, 292241, 292240, 292218, 292192, 292168, 292167, 292166, 292164, 292163, 292162, 292161, 292160, 292140, 292115, 292114, 292109, 292108, 292107, 292106, 292081, 292080, 292077, 292075, 292067, 292062, 292061, 292060, 292040, 292012, 291982, 291977, 291976, 291953, 291948, 291946, 291945, 291944, 291943, 291942, 291803, 291796, 291795, 291769, 291768, 291766, 291762, 291760, 291756, 291755, 291729, 291706, 291702, 291698, 291697, 291694, 291692, 291690, 291665, 291661, 291657, 291626, 291624, 291622, 291618, 291615, 291614, 291590, 291485, 291484, 291482, 291481, 291457, 291456, 291453, 291451, 291447, 291446, 291424, 291420, 291419, 291417, 291416, 291402, 291400, 291399, 291397, 291377, 291375, 291373, 291363, 291362, 291361, 291286, 291285, 291284, 291283, 291282, 291266, 291265, 291263, 291262, 291257, 291240, 291209, 291188, 291143, 291116, 291111, 291110, 291101, 291100, 291093, 291066, 291065, 291041, 291037, 291035, 291006, 291005, 291004, 291003, 291002, 290980, 290979, 290976, 290975,

290974, 290948, 290944, 290943, 290941, 290935, 290932, 290895, 290894, 290888, 290887, 290886, 290862, 290860, 290853, 290848, 290846, 290843, 290841, 290790, 290787, 290766, 290689, 290687, 290665, 290660, 290645, 290632, 290627, 290615, 290614, 290613, 290612, 290590, 290588, 290553, 290550, 290549, 290544, 290540, 290539, 290538, 290501, 290500, 290499, 290469, 290467, 290459, 290458, 290456, 290427, 290426, 290425, 290423, 290412, 290411, 290404, 290401, 290399, 290376, 290375, 290374, 290350, 290327, 290323, 290300, 290298, 290297, 290294, 290293, 290254, 290253, 290223, 290222,

LHC18o: RunList_LHC18o_pass2_MB (48 runs)
293368, 293386, 293392, 293413, 293424, 293474, 293475, 293494, 293496, 293497, 293570, 293571, 293573, 293578, 293579, 293582, 293583, 293587, 293588, 293686, 293689, 293690, 293691, 293692, 293695, 293696, 293698, 293740, 293741, 293770, 293773, 293774, 293776, 293799, 293802, 293805, 293806, 293807, 293809, 293829, 293830, 293831, 293856, 293886, 293891, 293893, 293896, 293898

LHC18p: RunList_LHC18p_pass2_MB (77 runs)

294925, 294916, 294884, 294883, 294880, 294877, 294875, 294852, 294818, 294817, 294816, 294815, 294813, 294809, 294805, 294775, 294774, 294772, 294769, 294749, 294746, 294745, 294744, 294743, 294742, 294741, 294722, 294721, 294718, 294716, 294715, 294710, 294703, 294653, 294636, 294634, 294633, 294632, 294620, 294593, 294591, 294590, 294588, 294587, 294586, 294563, 294562, 294558, 294556, 294553, 294531, 294530, 294529, 294527, 294526, 294525, 294524, 294503, 294502, 294310, 294307, 294305, 294242, 294241, 294212, 294210, 294208, 294205, 294201, 294200, 294199, 294156, 294155, 294154, 294152, 294131, 294128

LHC17h: RunList_LHC17h_pass2_MB (93 runs)
273103, 273100, 273099, 273077, 273010, 273009, 272985, 272983, 272976, 272949, 272947, 272939, 272935, 272934, 272933, 272932, 272905, 272903, 272880, 272873, 272871, 272870, 272836, 272834, 272833, 272829, 272828, 272784, 272783, 272782, 272764, 272763, 272760, 272749, 272747, 272746, 272712, 272692, 272691, 272690, 272620, 272610, 272608, 272607, 272585, 272577, 272575, 272574, 272521, 272468, 272466, 272463, 272462, 272461, 272413, 272411, 272400, 272399, 272395, 272394, 272389, 272388, 272360, 272359, 272340, 272335, 272194, 272156, 272155, 272154, 272153, 272152, 272151, 272123, 272101, 272100, 272076, 272042, 272041, 272040, 272039, 272038, 272036, 272020, 272018, 271886, 271881, 271880, 271874, 271873, 271871, 271870, 271868

LHC17i: RunList_LHC17i_pass2_MB (61 runs)

274442, 274390, 274389, 274388, 274387, 274386, 274385, 274364, 274363, 274360, 274352, 274351, 274329, 274283, 274281, 274280, 274278, 274276, 274271, 274270, 274269, 274268, 274266, 274264, 274263, 274259, 274258, 274232, 274212, 274174, 274148, 274147, 274125, 274094, 274092, 274064, 274058, 273986, 273985, 273946, 273943, 273942, 273918, 273889, 273887, 273886, 273885, 273825, 273824, 273719, 273711, 273709, 273695, 273690, 273689, 273687, 273654, 273653, 273593, 273592, 273591

LHC17k: RunList_LHC17k_pass2_MB (124 runs)

276508, 276507, 276506, 276462, 276439, 276438, 276437, 276435, 276351, 276348, 276312, 276307, 276302, 276297, 276294, 276292, 276291, 276290, 276259, 276257, 276230, 276205, 276178, 276177, 276170, 276169, 276166, 276145, 276140, 276135, 276104, 276102, 276099, 276098, 276097, 276045, 276041, 276040, 276020, 276019, 276017, 276013, 276012, 275925, 275924, 275847, 275664, 275661, 275657, 275650, 275648, 275647, 275624, 275623, 275622, 275621, 275617, 275612, 275559, 275558, 275515, 275472, 275471, 275467, 275459, 275457, 275456, 275453, 275452, 275448, 275443, 275406, 275404, 275401, 275395, 275394, 275372, 275369, 275361, 275360, 275333, 275332, 275328, 275326, 275324, 275322, 275314, 275283, 275247, 275246, 275245, 275239, 275188, 275184, 275180, 275177, 275174, 275173, 275151, 275150, 275149, 275076, 275075, 275073, 275068, 275067, 274979, 274978, 274886, 274882, 274878, 274877, 274822, 274821, 274817, 274815, 274811, 274807, 274806, 274803, 274802, 274801, 274708, 274690

LHC17l: RunList_LHC17l_pass2_MB (129 runs)

278216, 278215, 278191, 278189, 278167, 278166, 278165, 278164, 278163, 278158, 278127, 278126, 278123, 278122, 278121, 277996, 277991, 277989, 277987, 277952, 277930, 277907, 277904, 277903, 277901, 277900, 277899, 277898, 277897, 277876, 277870, 277848, 277847, 277845, 277842, 277841, 277836, 277834, 277805, 277802, 277801, 277800, 277799, 277795, 277794, 277749, 277747, 277746, 277745, 277725, 277723, 277722, 277721, 277577, 277576, 277575, 277574, 277537, 277536, 277534, 277531, 277530, 277479, 277478, 277477, 277476, 277473, 277472, 277418, 277417, 277416, 277389, 277386, 277385, 277384, 277383, 277360, 277314, 277312, 277310, 277293, 277262, 277257, 277256, 277197, 277196, 277194, 277193, 277189, 277188, 277184, 277183, 277182, 277181, 277180, 277155, 277121, 277117, 277091, 277087, 277082, 277079, 277076, 277073, 277037, 277017, 277016, 277015, 276972, 276971, 276970, 276969, 276967, 276920, 276917, 276916, 276762, 276675, 276674, 276672, 276671, 276670, 276644, 276608, 276557, 276556, 276553, 276552, 276551

LHC17m: Runlist_LHC17m_pass2_MB (109 runs)

280140, 280135, 280134, 280131, 280126, 280118, 280114, 280111, 280108, 280107, 280066,

280052, 280051, 279880, 279879, 279855, 279854, 279853, 279830, 279827, 279826, 279773, 279749, 279747, 279719, 279718, 279715, 279689, 279688, 279687, 279684, 279683, 279682, 279679, 279677, 279676, 279642, 279641, 279632, 279630, 279559, 279550, 279491, 279488, 279487, 279483, 279441, 279439, 279435, 279410, 279391, 279355, 279354, 279349, 279348, 279344, 279342, 279312, 279310, 279309, 279274, 279273, 279270, 279268, 279267, 279265, 279264, 279242, 279238, 279235, 279234, 279232, 279208, 279207, 279201, 279199, 279157, 279155, 279130, 279123, 279122, 279118, 279117, 279107, 279106, 279075, 279074, 279073, 279069, 279068, 279044, 279043, 279041, 279036, 279035, 279008, 279007, 279005, 279000, 278999, 278964, 278963, 278960, 278959, 278941, 278939, 278936, 278915, 278914

LHC17o: RunList_LHC17o_pass2_MB (155 runs)

281961, 281956, 281953, 281940, 281939, 281932, 281931, 281928, 281920, 281918, 281916, 281915, 281895, 281894, 281893, 281892, 281633, 281592, 281583, 281574, 281569, 281568, 281563, 281562, 281557, 281511, 281509, 281477, 281475, 281450, 281449, 281446, 281444, 281443, 281441, 281415, 281321, 281301, 281277, 281275, 281273, 281271, 281244, 281243, 281242, 281241, 281240, 281213, 281212, 281191, 281190, 281189, 281181, 281180, 281179, 281081, 281080, 281062, 281061, 281060, 281036, 281035, 281033, 281032, 280999, 280998, 280997, 280996, 280994, 280990, 280947, 280943, 280940, 280936, 280897, 280890, 280881, 280880, 280856, 280854, 280849, 280848, 280847, 280845, 280844, 280842, 280793, 280792, 280787, 280786, 280768, 280767, 280766, 280765, 280764, 280763, 280762, 280761, 280757, 280756, 280755, 280754, 280753, 280729, 280706, 280705, 280681, 280679, 280671, 280647, 280645, 280639, 280637, 280636, 280634, 280613, 280583, 280581, 280576, 280575, 280574, 280551, 280550, 280547, 280546, 280519, 280518, 280499, 280490, 280448, 280447, 280446, 280445, 280443, 280419, 280415, 280413, 280412, 280406, 280405, 280403, 280375, 280374, 280351, 280350, 280349, 280348, 280312, 280310, 280290, 280286, 280285, 280284, 280283, 280282

LHC17r: RunList_LHC17r_pass2_MB (30 runs)

282704, 282703, 282702, 282700, 282677, 282676, 282673, 282671, 282670, 282668, 282667, 282666, 282653, 282651, 282629, 282622, 282620, 282618, 282609, 282608, 282607, 282606, 282580, 282579, 282575, 282573, 282546, 282545, 282544, 282528